Doctoral Dissertation

Electrochemical Properties of Co-Sintered Anode Materials with Oxide-Based Solid Electrolyte for Solid-State-Battery

（全固体電池実現に向けた酸化物系固体電解質を用いた共焼結負極材料の電気化学的特性）

January 2024

Yoichiro Kawano

Department of Chemistry and Biotechnology

Graduated School of Engineering

Tottori University

Preface

The following experiment was conducted under the guidance of Professor Hiroki Sakaguchi, Associate Professor Hiroyuki Usui, and Associate Professor Yasuhiro Domi at the Applied Chemistry Course, Department of Chemistry and Biotechnology, Graduated School of Engineering, Tottori University between 2022 and 2024.

The purpose of this study was to elucidate the electrochemical characteristics after co-sintering the oxide-based solid electrolyte and anode materials. The findings obtained in this experiment are expected to promote the development of input/output characteristics and high-energy-density batteries for all-solid state battery.

Yoichiro Kawano

Department of Chemistry and Biotechnology

Graduate School of Engineering

Tottori University

4-101 Minami, Koyama-cho, Tottori 680-8552, Japan

January 2024

Content

General Introduction

The latest lithium-ion secondary batteries have high energy density, making them suitable for high-energy-demanding applications such as portable devices and electric vehicles, thereby extending device operation and improving electric vehicle range. They also offer a longer lifespan compared to traditional batteries, reducing the frequency of replacements while maintaining sustained performance. Lithium-ion batteries exhibit high charge/discharge efficiency, resulting in shorter charging times and efficient energy utilization. The combination of solar power and storage batteries is expected to help build a society that uses clean energy without emitting greenhouse gases.

However, lithium-ion batteries contain a flammable organic electrolyte, making it even more difficult to maintain safety in high energy density batteries.[1,2] The safety concerns, including the risk of fire and explosions due to overcharging and physical damage, require ongoing research and design improvements. There are also energy density limits, which may not meet the demands of certain applications, thus driving the need for the development of next-generation battery technologies. Additionally, in order to realize a sustainable society, it is necessary to select materials that are cost-effective and non-toxic. The construction of recycling systems is also an important subject of research.[3,4]

Therefore, there has been growing interest in all-solid-state batteries because

of the excellent manufacturing safety owing to their non-flammable solid electrolytes. A solid

electrolyte is a solid substance that conducts electricity through the movement of ions within

its structure. Especially, ceramic solid electrolytes are expected to be applied to the next

generation of batteries.[5,6,7] These are typically oxides, sulfides, or mixed ionic conductors.

Examples include lithium phosphates, lithium ceramics,[8,9,10] and sulfide-based

materials.[11,12,13] However, the manufacturing process is different from that of conventional

lithium-ion batteries, and finding optimized the conditions for each solid electrolyte is an

important issue. For instance, the sintering process is necessary to conduct the oxide-based

solid electrolyte. Unexpected resistive layers may be generated during the sintering process,

reducing charge/discharge capacity or current density. That's reason why it is important to

clarify solid electrolyte and active materials conditions after sintering.

We focused on oxide-based solid electrolyte which is the Na super ionic

conductor (NASICON) -type $Li_{1.5}Al_{0.5}Ge_{1.5}(PO_4)_3$ (LAGP). The solid electrolyte must

function as a conductor of Li in the charge/discharge reaction of solid-state batteries, and the

sintering conditions necessary for this oxide-based solid electrolyte.[14,15,16,17] LAGP exhibits

good Li conductivity when sintered from the amorphous phase to the crystalline phase.

However, it has been reported that co-sintering LAGP with active materials at temperatures

as high as 1000 °C results in the formation of reaction phases that inhibit Li conductivity. In

5

this study, we evaluated the crystal structure and electrochemical properties of LAGP co-sintered at lower temperatures than 900 °C and investigated appropriate sintering conditions. We conducted the analysis of LAGP, which was sintered at various temperatures to investigate its ionic conductivity and potential windows.

Secondly, we revealed the charge/discharge characteristics of a battery prepared by co-sintering LAGP and titanium dioxide (TiO_2) anode materials. TiO_2, which is widely used for paints and photocatalysts, is a relatively abundant resource, and its use as anode material in secondary batteries would enable cost-effective and non-toxic batteries. The theoretical capacity per weight of titanium dioxide is 335 mA h g^{-1}, comparable to graphite's 372 mA h g^{-1}. In addition, the theoretical capacity per volume is 1266 mA h cm^{-3} of anatase-type TiO_2 and 1417 mA h cm^{-3} of rutile-type TiO_2, exceeding the theoretical value of 837 mA h cm^{-3} of graphite. TiO_2 structure have polymorphs, especially anatase-type TiO_2, which has been investigated earlier. On the other hand, rutile-type TiO_2 is known to have Li^+ diffusion five orders higher than anatase-type TiO_2 and a strong crystalline structure.[18] In this study, we examined rutile-type TiO_2, which is considered to be the most stable structure and can maintain its crystal structure and Li^+ diffusion ability even when co-sintered with LAGP.

Finally, we investigated the analysis of reaction phase of LAGP solid electrolytes co-sintered with silicon and silicide-based anode materials, the electronic

conductivity before and after sintering, and the charge/discharge characteristics of the fabricated batteries. Silicon is a very attractive anode material for the construction of high-energy-density batteries because there is no concern about resource depletion and it has a theoretical capacity (3600 mA h g^{-1}) that is more than 10 times that of current graphite-based anode materials.[19,20] However, its low electronic conductivity and large expansion and contraction during charge/discharge make it difficult to use as an anode material. In this study, we focused on silicide materials, which has excellent electronic conductivity, thermoelectric conductivity, and mechanical strength. It was investigated reaction phase when co-sintered with LAGP, changes in electronic conductivity, charge/discharge characteristics of sintered electrode sheets, and products during charge/discharge process.

This thesis is structured as follows.

Chapter 1: We evaluated the current density of the redox decomposition of the NASICON-type LAGP containing amorphous phase. The cyclic voltammetry measurements was performed to conform the current density each voltage of LAGP.

Chapter 2: We investigated the charge/discharge characteristics of the sintered multilayer oxide-based all-solid-state batteries using TiO$_2$ anode materials. It was conducted that charge/discharge evaluations to clarify the capacity at high current density the cell using rutile-type TiO$_2$ or anatase-type TiO$_2$.

Chapter 3: We analyzed the reaction phase which is silicone and silicide anode materials co-sintered with oxide-based solid electrolyte, and electrochemical behavior. It was explored the reaction phases and the charge/discharge behavior after co-sintering with LAPG and various silicon and silicide anode materials.

Lastly, we present our concluding remarks.

Chapter 1

NASICON-type $Li_{1.5}Al_{0.5}Ge_{1.5}(PO_4)_3$ Containing Amorphous Phase for Solid Li-Ion Conductor

1.1 Introduction

All-solid-state batteries have emerged as a response to the escalating demands for rechargeable batteries, specifically aiming to enhance energy density. The anticipated rise of all-solid-state oxide batteries as the next generation in this realm is rooted in their exceptional safety features and outstanding resistance to oxidation, particularly under high voltages. Our research endeavors have centered on oxide-based solid electrolytes, specifically focusing on sintered multilayer oxide-based all-solid-state batteries utilizing a Na super ionic conductor (NASICON)-type solid electrolyte, $Li_{1.5}Al_{0.5}Ge_{1.5}(PO_4)_3$ (LAGP).[21] A noteworthy characteristic of LAGP indicates in its ability to achieve a crystalline phase through sintering at approximately 650 °C, showing an ionic conductivity of 1×10^{-5} S cm^{-1} at 25 °C.[22] This unique lithium-ion conductivity of LAGP emerges from the transition between its amorphous and crystalline phases, facilitated during the sintering process. Regarding electrochemical stability, experimental data indicates a reductive decomposition reaction at low potentials, resulting in the formation of germanium (Ge) alloys with lithium (Li), eventually transforming into LiGe, suggesting a Li deinsertion reaction in organic electrolyte solution-

based cells.[23] Conversely, LAGP exhibits excellent stability at high potentials of 5 V vs. Li$^+$/Li.

Additionally, comparative studies highlight LAGP's superior redox resistance in contrast to

$Li_{1.3}Al_{0.7}Ti_{1.7}(PO_4)_3$ (LATP) when both are evaluated as NASICON-based solid electrolytes.[24]

The preparation of the amorphous phase of LAGP involves melting the raw material

at 1300 °C, followed by rapid quenching.[22] The amorphous phase transitions to a crystalline

state at around 600 °C. However, investigations indicate that both the temperature of this

phase transition and the resultant substances vary based on the quantity of incorporated

aluminum (Al) in the system.[25] In order to analyze the structure of LAGP in the advanced

stage of crystallization, Raman measurements of LAGP crystallized in the temperature range

of 750-850°C were performed.[26] These measurements confirmed the transition of the

amorphous phase to the crystalline state at 625 °C. Notably, when crystallized at 820 °C, the

highest measured ionic conductivity at 25 °C reached 3.9×10^{-4} S cm^{-1}. Moreover, it has

been observed that conducting the crystallization process at temperatures exceeding 820 °C

leads to a decline in ionic conductivity attributed to the formation of GeO_2 and voids within

the sintered compounds.

To leverage the favorable traits of LAGP in all-solid-state batteries, it's pivotal to

minimize the generation of reaction products during the co-sintering process with the active

material. This necessitates sintering solid electrolytes at the lowest feasible temperature.

Various strategies have been explored to enhance LAGP's sinterability, such as integrating Li₃BO₃ as a sintering aid and applying shorter-duration, high-pressure conditions during the sintering process.[27] While the activation energy required for Li^+ conduction in crystallized LAGP was found to be approximately 0.4 eV, the presence of sintering aids poses a significant challenge by reducing ionic conductivity of solid electrolyte. Previous investigations aimed at crystallizing LAGP at lower temperatures revealed that the crystallization temperature of amorphous LAGP could be reduced below 610 °C by adjusting temperature ramp rates during sintering.[28] Specifically, employing temperature increase rates of 3, 5, 8, and 10 °C min⁻¹ effectively lowered the crystallization temperature. In a study involving 50 minutes sintering duration, thermal analysis determined an activation energy requirement for Li^+ conduction of 378 kJ mol⁻¹. These findings suggested inadequate progress in LAGP crystallization, resulting in a high activation energy due to the substantial presence of the amorphous phase. Both studies underscore multiple uncertainties in analyzing and measuring ionic conductivity in LAGP, particularly in relation to the sintering process around 600 °C, wherein both amorphous and crystalline LAGP coexist.

The potential for producing all-solid-state batteries with minimized impurity phase formation alongside electrochemical stability emerges if LAGP can crystallize at lower temperatures. To explore this possibility, we delved into the electrochemical properties of

LAGP sintered at 600 °C, where both crystalline and amorphous phases coexisted. Our investigation focused on evaluating the visual appearance and ionic conductivity of sintered crystallized LAGP by varying sintering conditions, including atmosphere, temperature, and retention time, using solely amorphous LAGP. Furthermore, we scrutinized the elemental composition ratios of sintered LAGP that underwent crystallization at temperatures of 600 °C or 800 °C. This analysis aimed to discern any alterations resulting from different crystallization temperatures. Additionally, we conducted an assessment of the current density related to the redox decomposition in the Li metal counter electrode. These comprehensive examinations aimed to elucidate the potential of manipulating sintering conditions to control the crystallization process and subsequent properties of LAGP for optimized application in all-solid-state batteries.

1.2 Experimental

We utilized a white amorphous powder of $Li_{1.5}Al_{0.5}Ge_{1.5}(PO_4)_3$ obtained from Toshima Manufacturing, Ltd., characterized by a particle size (D_{50}) of 0.5 μm and a purity level of 99.9 %. This material served as the base for preparing the sintered sheets. To produce the unsintered sheet (as the green sheet), a blend of amorphous LAGP, polyvinylidene difluoride (PVDF), and anhydrous isopropanol was formulated in a weight ratio of 20:30:50.

The mixture underwent a 20 hours ball milling process and was subsequently vacuum-defoamed. The resulting paste was coated onto a polyethylene terephthalate (PET) film using the doctor-blade method and dried at 150 °C in a dryer to evaporate the solvent. Stacking multiple green sheets together and applying pressure yielded the desired electrolyte layer thickness, resulting in a final laminated green sheet measuring 300 μm in thickness. After crimping, the sheet was cut to a size of 20 mm × 20 mm to form the white electrolyte layer green sheet.

We explored various sintering conditions by manipulating both the sintering temperature and retention time within nitrogen and air atmospheres. The temperature ramp-up rate was set at 100 °C per minute across all conditions. Sintering in a nitrogen atmosphere was executed at a consistent temperature of 600 °C for a duration of 2 hours. Conversely, in an air atmosphere, the sintering process involved the following temperature and duration parameters: 600 °C for 2 hours, 700 °C for 2 hours, 700 °C for 20 hours, 800 °C for 2 hours, and finally, 900 °C for 2 hours.

Figure 1-1 (a) displays the schematic representation of the impedance cell used in the study. Impedance measurements were carried out employing an impedance apparatus (SP-300 Potentiostat, Bio-Logic Science Instruments). Gold (Au) electrodes, 10 mm in diameter, were applied to both sides of the sintered LAGP sheet. The frequency range explored spanned

from 7 MHz to 0.1 Hz with an applied amplitude of 5 mV. Analysis of the Nyquist plots

enabled the determination of resistances Rs and Rp. Rs denotes the bulk resistance within the

solid electrolyte particles, while Rp represents the interfacial resistance between these

particles.

The cell setup for cyclic voltammetry, illustrated in Figure 1-1 (b), was employed to

determine the potential window of LAGP. Using the SP-300 equipment, measurements were

conducted. An Au-coated electrode was prepared on one side of the sintered LAGP sheet.

Subsequently, a polymer electrolyte (Osaka soda) containing lithium

bis(trifluoromethanesulfonyl)amide (LiTFSA) with an 80 μm thickness underwent vacuum

drying at 80 °C for 12 hours in a glove box dryer. This polymer electrolyte was placed

between the solid electrolyte and lithium metal. The lithium metal, cut into a square shape

with sides measuring 22 mm, was attached to a copper foil. Assembly of the test cell involved

laminating the sintered LAGP sheet, the polymer electrolyte (Osaka soda), and the lithium

metal connected to a copper foil. Cyclic voltammetry measurements were conducted over

four cycles at a sweep rate of 1 mV s^{-1}. The voltage ranged from an initial increase of 3 V to

6 V, followed by a decrease to 0 V, and subsequently, an increase back to 3 V. Current density

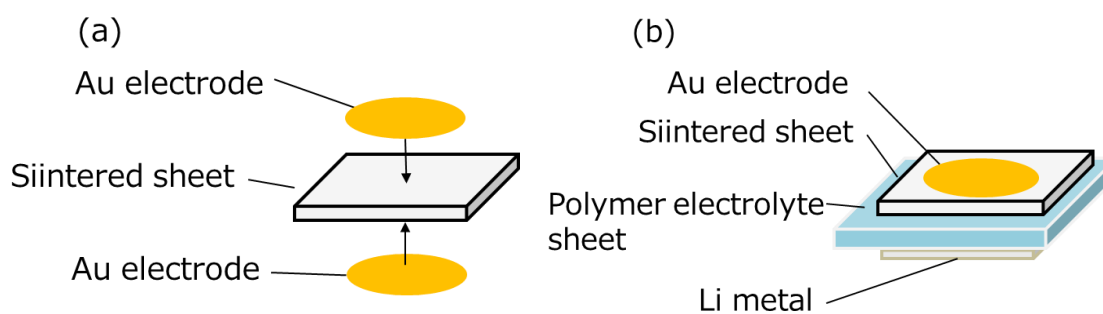was recorded during these operations.

Figure 1-1. Configuration diagram of the cell used for (a) impedance measurements and (b) Cyclic voltammograms.

For electronic conductivity measurement, the same instrumentation and samples utilized in the impedance measurements were employed. Initial resistance was calculated using the equation $V = IR$, with current values measured across voltages ranging from ± 0.1 to 0.5 V and a retention time of 300 seconds. Conductivity was subsequently determined by integrating obtained resistance values with the thickness and area of each sample. Finally, the electronic conductivity was derived as the reciprocal of the conductivity.

Crystal structure analysis was conducted using an X-ray diffraction (XRD) system equipped with a CuKα X-ray source (SmartLab, Rigaku Corp.). The observed XRD patterns of the LAGP matched with the diffraction pattern of the NASICON $LiGe_2(PO_4)_3$ trigonal (ICSD No. 69763) in the R-3c space group.

Raman spectra of both amorphous and crystalline phases within the sintered LAGP sheets were obtained using a microscopic laser Raman spectrometer (LabRAM HR Evolution

VIS-NIR, HORIBA, Ltd.). Measurements spanned from 200 to 1200 cm^{-1} with a laser wavelength of 457 nm. Each data point was recorded with an exposure time of 1 second, and the spectra were averaged from four integrations. Raman mapping results for the sintered LAGP sheets were normalized using the Raman peak 447 cm^{-1} characteristic of the LAGP crystalline phase.

Elemental analysis was conducted employing inductively coupled plasma optical emission spectrometry (ICP-OES) (720-ES, Varian) after crushing the sintered material in a mortar. The resulting powder underwent dissolution in a mixture of nitric, hydrochloric, and hydrofluoric acids and subsequent microwave treatment. A boric acid solution was added to explore the oxygen content in more detail. Further analysis of oxygen content was performed using an oxygen nitrogen hydrogen analyzer (ONH836, LECO Japan).
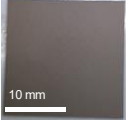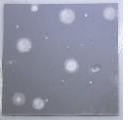
1.3 Results and Discussion

Table 1-1 presents the visual appearance of sheets sintered under different atmospheres, temperatures, and retention times, along with their respective ionic conductivities acquired from alternating current (AC) impedance measurements and electro conductivities calculated via direct current (DC) resistance. Notably, sheets containing amorphous LAGP phase prior to sintering showed no discernible ionic conductivity. However,

16

after sintering, all LAGP sheets exhibited approximately 10^{-5} S cm^{-1} in ionic conductivity. The morphological characteristics of the sintered sheets displayed notable variations corresponding to distinct sintering conditions.

Table 1-1. Appearance, ion and electronic conductivity of sintered amorphous LAGP sheet under various atmospheres, temperatures, and retention times.

Sample number	Green Sheet	1	2	-	-	3	-
Atmosphere	-	N$_2$	Air	Air	Air	Air	Air
Sintering temp. / ℃	-	600	600	700	700	800	900
Retention time / h	-	2	2	2	20	2	2
Appearance (after sintering)							
R_s / Ω	unmeasurable	254.8	222.1	336	149.2	216.8	552.2
R_p / Ω	unmeasurable	1238	1142	902.9	345	235.4	361
Ion conductivity at 25 ℃ / S cm^{-1}	unmeasurable	2.6×10^{-5}	2.8×10^{-5}	3.1×10^{-5}	7.7×10^{-5}	8.4×10^{-5}	4.2×10^{-5}
Electronic conductivity at 25 ℃ / S cm^{-1}	-	2.0×10^{-9}	1.6×10^{-9}	-	-	3.0×10^{-9}	-

These differences in visual appearances were noted based on various sintering conditions: nitrogen sintering at 600 °C resulted in brown-colored sheets, while air sintering produced gray-colored ones. Despite comparable ionic conductivities and no discernible differences in bulk (Rs) and interface resistances (Rp), the color change was attributed to the formation of a mixture of amorphous and crystalline phases in the sintered sheets at 600 °C. At 700 °C, the sheets turned light gray, and those held for 20 hours displayed white dots within the gray coloration. The ionic conductivity doubled with a 20 hours retention

17

compared to 2 hours, indicating increased sintering and crystallization of LAGP. Sintering at 800 °C yielded completely white sheets with the highest ionic conductivity, whereas at 900 °C, a decrease in ionic conductivity occurred due to the presence of bubbles, likely originating from LAGP softening and subsequent crystallization with air release. Electro conductivity analysis consistently indicated low conductivities ($10^{-9}\,\text{S cm}^{-1}$) across all sintering conditions for LAGP sheets.

Figure. 1-2 (a) and (b) shows the XRD and Raman analysis results of the amorphous LAGP powder before sintering and the sintered sheets obtained by sintering at 600 °C in nitrogen (sample No. 1), 600 °C in air (No. 2), and 800 °C in air (No. 3). The XRD findings verified the emergence of a crystalline phase of LAGP alongside the presence of minor GeO_2 impurities. Previous studies have suggested that GeO_2 is an impurity phase formed when sintering amorphous LAGP above 750 °C. [22,25] GeO_2, with a melting point of around 1100 °C, typically adopts an amorphous phase. The preparation of the LAGP amorphous phase involves mixing raw materials and rapidly cooling the melt at approximately 1300 °C. Small amounts of amorphous GeO_2 likely formed during this process and are believed to have crystallized. This succinctly encapsulates the formation of crystalline LAGP alongside GeO_2 impurities and their relationship in the sintering process, detailing their amorphous phase formation and subsequent crystallization.
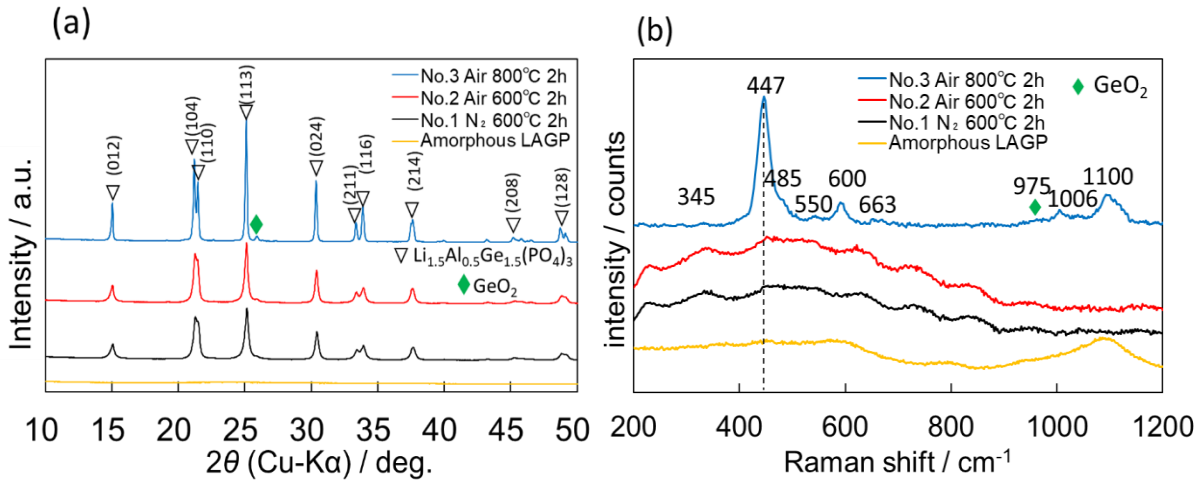
Figure 1-2. (a) XRD and (b) Raman measurements of sintered amorphous LAGP sheet samples 1, 2, and 3.

The XRD analysis revealed that the diffraction peaks of the LAGP crystalline phase were notably sharper in the 800 °C sintered sheets compared to those at 600 °C. Calculations using the Scherrer formula for crystallite size indicated sizes of 27.7 nm (No. 1), 34.7 nm (No. 2), and 69.4 nm (No. 3), showing an increase in size with higher sintering temperatures. Raman spectroscopy results at 600 °C displayed broad peaks indicative of amorphous LAGP in the wavenumber range of 200-1000 cm^{-1} across all sintering atmospheres. However, LAGP sintered at 800 °C exhibited distinct peaks corresponding to LAGP crystalline and minor GeO$_2$ impurity phases.[26]   Despite the laser wavelength variation to 532 nm, no alterations in peak shapes for crystalline and amorphous LAGP were noted (Figure 1-3 a,b). The chosen 457 nm wavelength aimed at minimizing Raman shift noise.   Raman mapping

indicated the presence of connected LAGP crystalline particles, suggesting a mixture of

amorphous and crystalline phases in the LAGP sintered at 600 °C (Figure.1-4 (a), (b), and

(c)). It suggested that the LAGP sintered at 600 °C has a mixture of amorphous and crystalline
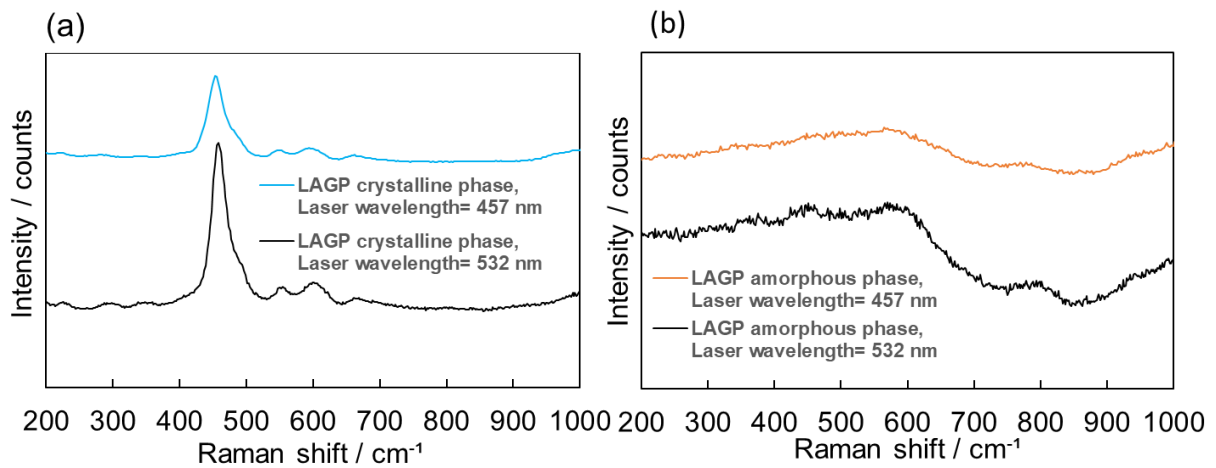
phases.

Figure 1-3. Raman measurements of (a) LAGP crystalline phase and (b) amorphous phase at
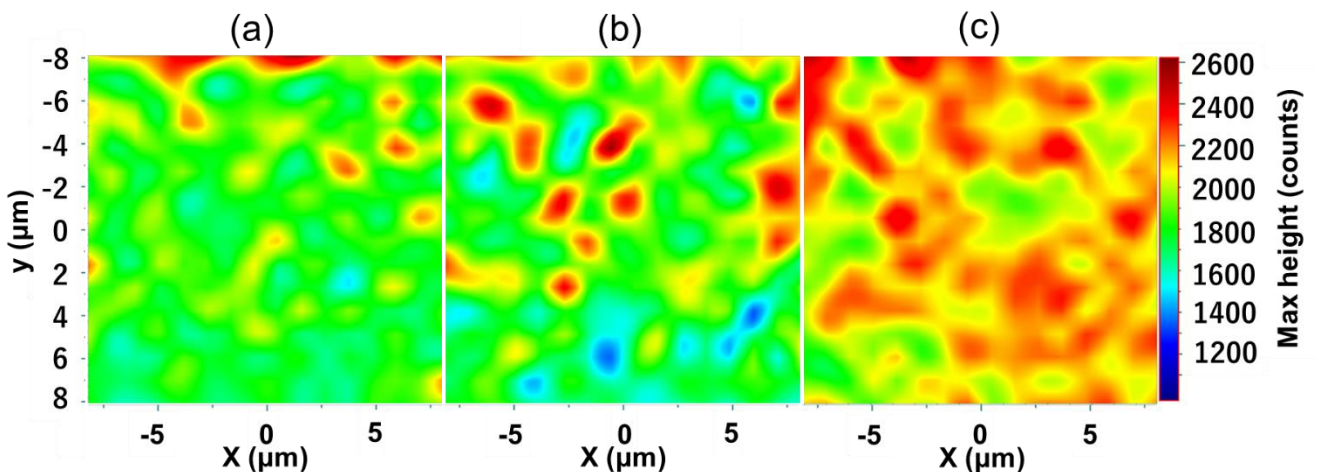
different laser wavelengths.

Figure 1-4. Raman mapping measurements of sintered amorphous LAGP sheet samples

(a) 1, (b) 2, and (c) 3.

Table 1-2 presents the ICP-OES measurements and oxygen content analysis for

LAGP sintered samples 1, 2, and 3, alongside reference data for crystalline LAGP powder

sourced from Toshima Manufacturing, Ltd. Analysis of the ICP results revealed a slight

deficiency in lithium content in the 600 °C-sintered sheet, regardless of the sintering

atmosphere, while the 800 °C-sintered sample exhibited a composition ratio akin to the

standard sample. Notably, the lithium deficient structure within a solid electrolyte typically

augments ionic conductivity.[29] However, in our investigation, we did not observe a

discernible increase in ionic conductivity in the lithium deficient LAGP. This observation

may be attributed to the composite of the LAGP sheet, consisting of both amorphous and

crystalline phases sintered at 600 °C.

Table 1-2. ICP-OES measurements (Li, Al, Ge, and P), oxygen content analysis (O) of LAGP

sintered samples 1, 2, and 3 (Molar ratios are given for Li, Al, Ge, and P, and weight

percentage values for O.)

	Sintering process		ICP analysis				O analysis
Sample number	Atmosphere	Temp. / ℃	Li	Al	Ge	P	O / wt%
Reference	-	-	1.5	0.5	1.5	3	45.96
1	N$_2$	600	1.44	0.53	1.44	2.97	44.5
2	Air	600	1.44	0.5	1.42	2.94	46.4
3	Air	800	1.5	0.56	1.44	2.97	46.2

The oxygen content analysis results revealed that the oxygen contents of samples sintered in air (No. 2 and 3) were comparable to that of the standard sample (45.96 wt%). In contrast, the sample sintered in a nitrogen atmosphere (No. 1) exhibited a slight deficiency in oxygen. Previous studies have shown that the crystal structure and electronic conductivity of oxides, like TiO_2, can be enhanced by introducing dopant elements, leading to an oxygen-deficient structure.[30] However, despite the nitrogen-sintered LAGP (No. 1) displaying oxygen deficiency, there was no observed improvement in electronic conductivity in our study (Table 1-1)

Cyclic voltammetry (CV) measurements were conducted over four cycles to explore the influence of crystallinity and composition variations among LAGPs on their electrochemical properties (Figure 1-5). Figure 1-6 provides a detailed depiction of CV curves during the 1st and 4th cycles for samples 1, 2, and 3 to elucidate the dataset further. The CV experiments initiated at 3 V vs. Li^+/Li, gradually reaching voltages up to 6 V vs. Li^+/Li. During voltage application, observed current responses corresponded to oxidative decomposition reactions. Subsequently, a reverse voltage sweep from 6 V to 0 V vs. Li^+/Li induced current behavior aligned with reductive decomposition reactions. Moreover, the voltage ramp from 0 V to 3 V vs. Li^+/Li demonstrated current behaviors attributable to the redox reactions of the reductive decomposition products. This behavior, previously

documented in literature,[23] is believed to stem from the $Li_xGe \rightarrow Ge + xLi^+ + xe^-$ dealloying reaction. Each of these steps constituted a single cycle, and comparisons of redox currents were drawn after four cycles of CV measurements. In both sintered materials, a marginal current indicative of oxidative decomposition was noticeable at elevated potentials from the initial stages, implying that LAGP does not exhibit complete stability as a solid electrolyte under high potentials. Additionally, on the reduction side, consistent with prior research,[3] significant behavior associated with reductive decomposition from approximately 1 V vs. Li^+/Li was observed, deteming LAGP's diminished stability as a solid electrolyte.
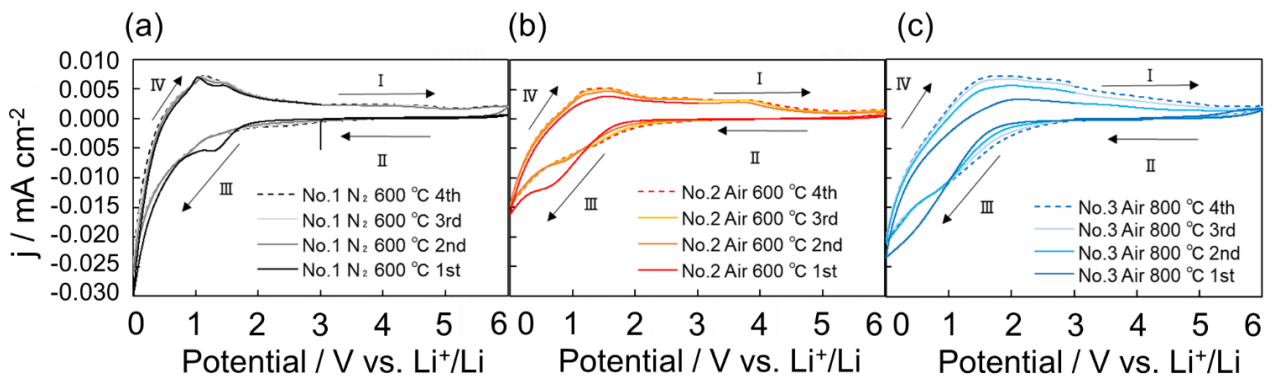

Figure 1-5. Cyclic voltammograms (cycles 1-4) for sample (a) No. 1, (b) 2, and (C) 3.
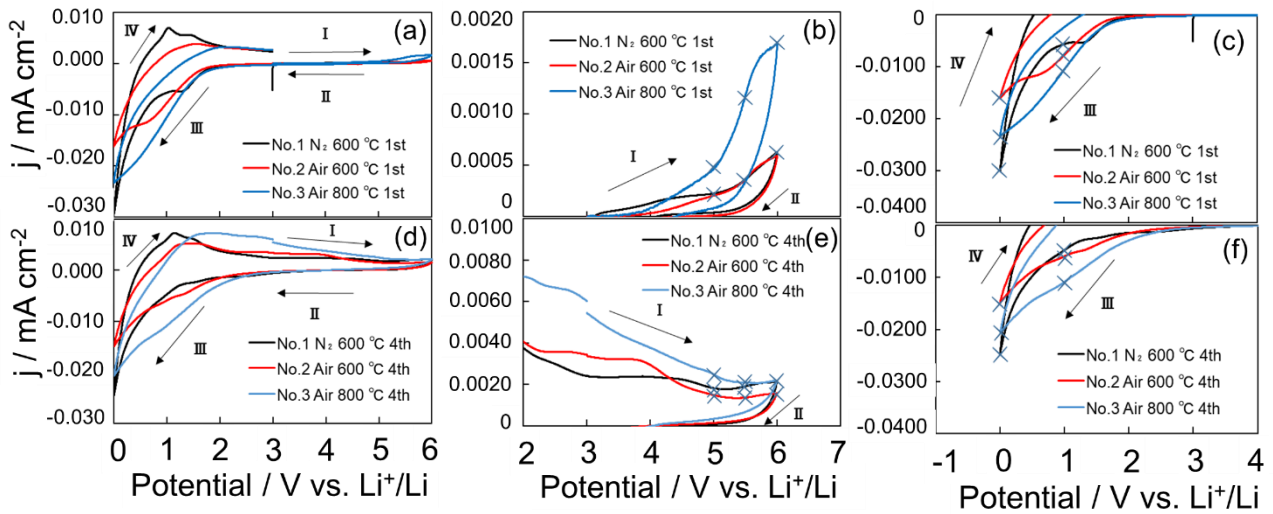
Figure 1-6. Cyclic voltammograms for the (a) 1st cycle, (b) oxidative decomposition side at 1st cycle, (c) reductive decomposition side at 1st cycle, (d) 4th cycle, (e) oxidative decomposition side at 4th cycle, and (f) reductive decomposition side at 4th cycle of samples 1, 2, and 3 (X in the figure indicates the current density measurement points at 0, 1.0, 5.0, 5.5, and 6.0 V vs. Li$^+$/Li).

The findings presented in Table 1-3 outlined the current densities observed at 5, 5.5, and 6 V vs. Li$^+$/Li during oxidation, and at 0 and 1 V vs. Li$^+$/Li during reduction. The 800 °C-sintered sheet (No. 3) exhibited the highest current density on the oxidation side, whereas the values for the 600 °C-sintered sheets (No. 1 and No. 2) remained similar irrespective of the sintering atmosphere. This observation indicates a suppression of oxidative decomposition in

the 600 °C-sintered sheets at high potentials. The superior ionic conductivity noted in the LAGP calcined at 800 °C is attributed to vacancy formation within the LAGP crystal structure due to partial Li loss in the highly crystalline LAGP. This vacancy formation might have contributed to reduced oxidation resistance at high potentials. Conversely, the presence of a mixture of amorphous and crystalline phases in the LAGP sintered at 600 °C potentially restrains the oxidative decomposition of the solid electrolyte. Comparatively, the current values observed during reduction were notably higher than those during oxidation. Particularly, the 600 °C-sintered sheet in a nitrogen environment (No. 1) displayed the smallest value at approximately 0.5 V vs. Li^+/Li. After four cycles, a decline in redox current density was noted. It's imperative to consider the behavior during the 4th redox cycle, as it represents the current behavior of LAGP subsequent to the application of a voltage spanning 0 to 6 V Li^+/Li.

Table 1-3. Current densities at specific potentials in the 1st and 4th cycles of samples 1, 2, and 3. (Current densities at 0 and 1.0 V vs. Li^+/Li on the reducing side and 5.0, 5.5, and 6.0 V vs. Li^+/Li on the oxidizing side are noted.)

	Current density at the 1st cycle / mA cm^{-2}				
Sample number	5 V	5.5 V	6 V	1 V	0 V
1	2.2×10^{-4}	3.6×10^{-4}	6.3×10^{-4}	-5.7×10^{-3}	-3.0×10^{-2}
2	2.0×10^{-4}	3.7×10^{-4}	5.9×10^{-4}	-7.7×10^{-3}	-1.6×10^{-2}
3	4.7×10^{-4}	1.2×10^{-3}	1.7×10^{-3}	-1.1×10^{-2}	-2.3×10^{-2}

	Current density at the 4th cycle / mA cm^{-2}				
Sample number	5 V	5.5 V	6 V	1 V	0 V
1	1.8×10^{-3}	1.9×10^{-3}	2.1×10^{-3}	-4.7×10^{-3}	-2.5×10^{-2}
2	1.5×10^{-3}	1.4×10^{-3}	1.6×10^{-3}	-5.9×10^{-3}	-1.5×10^{-2}
3	2.5×10^{-3}	2.1×10^{-3}	2.2×10^{-3}	-1.1×10^{-2}	-2.1×10^{-2}

The redox mechanism is elucidated through first-principles calculations of the density of states of the constituent elements within LAGP, as depicted in Figure 1-7. On the oxidation side, the influence of oxygen (O) at the top of the valence band is expected to result in oxygen emission. Conversely, for the reduction side, a reduction of GeO is anticipated due to the substantial impact on both germanium (Ge) and oxygen (O) positioned at the lowest level of the conduction band. The amorphous form of LAGP is anticipated to possess a short-period crystalline structure akin to commonly reported glassy structures. In well-crystallized LAGP, first-principles calculations indicate the presence of oxygen atoms at the upper end of the valence band. However, in amorphous LAGP, this position is projected to shift. We hypothesize that this shift may act to suppress oxidative decomposition
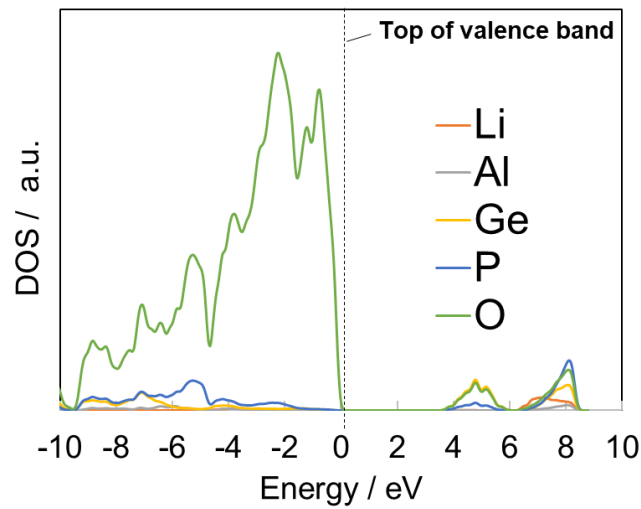
Figure 1-7. Density of state calculated for LAGP crystalline phase.

Calculation conditions

Software: Quantum espresso (https://www.quantum-espresso.org/)

Approximation method: Density functional method (especially pbesol)

Analysis method: Plane wave basis + pseudopotential (Ultrasoft pseudopotential)

Cutoff energy: 90 Ry (for wave function expansion) 1000 Ry (for density expansion)

K-point mesh: SCF: 3 × 3 × 2 DOS: 5 × 5 × 2

Previous reports on amorphous solid electrolytes, such as Li_2S-P_2S_5, have highlighted their high ionic conductivity, emphasizing their potential in sulfide-based solid electrolytes.[31] This study suggests that while amorphous LAGP may not exhibit significant ionic conductivity, it could contribute to stabilizing the operation of oxide-based solid electrolytes.

27

The impact of sintering atmosphere is noteworthy. Exposure to air during sintering has been reported to attract lithium to NASICON solid electrolyte particle surfaces, reducing internal lithium concentration.[32] Although atmospherically sintered LAGP enhances ionic conductivity through vacancy introduction, this process might compromise electrochemical stability at high potentials. Raman results at 600 °C sintering indicate a mixed amorphous and crystalline structure in LAGP, suggesting structural modifications for enhanced stability at high potentials. This study demonstrates that lowering the sintering temperature from 800 °C to 600 °C results in LAGP sintered sheets with a combination of amorphous and crystalline phases, effectively suppressing oxidation decomposition reactions at high potentials. Variations in cyclic voltammetry measurements align with the inclusion of amorphous LAGP and the disparity in vacancy formation in the LAGP crystalline phase, contingent upon the sintering atmosphere. However, the standalone electrochemical stability of amorphous LAGP remains unexplored. Future investigations will focus on evaluating its impact at solid-state interfaces.

1.4 Summary

This investigation centered on exploring the ionic conductivity and electrochemical traits of LAGP sintered under diverse temperatures and atmospheres. LAGP amorphous

sheets sintered at 600 °C exhibited a brown or gray color, displaying an approximate ionic conductivity of 2×10^{-5} S cm^{-1}. In contrast, sheets sintered at 800 °C resulted in a white appearance. Interestingly, samples sintered at 700 °C for 20 hours and those at 800 °C displayed an augmented ionic conductivity, reaching roughly 8×10^{-5} S cm^{-1}. The visual change from amorphous to a mixed phase of amorphous and crystalline states corresponded to discoloration, as observed in appearance photographs. XRD measurements affirmed that the principal phase in all LAGP samples remained crystalline. Additionally, Raman spectroscopic analyses supported the presence of the amorphous phase specifically in the LAGP sample sintered at 600 °C. The ionic conduction mechanism in sintered materials containing amorphous phases seems to rely on sustaining ionic conductivity via the formation of a three-dimensional network involving LAGP crystalline phases within the solid electrolyte layer, as suggested by Raman mapping results. Cyclic voltammetry measurements underscored that LAGP sintered at 600 °C exhibited lower current density at high potentials, indicating potential suppression of oxidative decomposition. ICP-OES and oxygen content analysis results further indicated deviations in lithium and oxygen levels from the theoretical ratio in LAGP sintered at 600 °C. The cyclic voltammetry readings showed alterations in current density due to the inclusion of the amorphous LAGP phase and variability in vacancy formation states within the LAGP crystalline phase, contingent upon the calcination

atmosphere.

The outcomes of this study hold substantial importance as they contribute to bolstering the stability of charge/discharge cycles through the incorporation of an amorphous LAGP phase within the solid electrolyte. This enhancement holds particular relevance in systems employing high-voltage cathode materials alongside a solid LAGP electrolyte. Similar beneficial effects were noted in an all-solid-state battery, aligning with observations from our prior research.[33] While the complete mechanism behind the alteration in ionic conductivity remains elusive, we consider the application of this knowledge in industrial technology to be crucial. For sintered materials exhibiting a blend of amorphous and crystalline phases, our forthcoming analysis will delve into local structural changes via pair distribution function (PDF) analysis and assess band gap alterations obtained from diffuse reflection spectra. In our future research endeavors, we aim to investigate solid-state interfaces extensively, employing Scanning Transmission Electron Microscopy (STEM) to gain deeper insights and comprehension.

Chapter 2

TiO$_2$ Anode Material for All-Solid-State Battery Using NASICON Li$_{1.5}$Al$_{0.5}$Ge$_{1.5}$(PO$_4$)$_3$ as Lithium Ion Conductor

2.1 Introduction

Lithium-ion secondary batteries, employing nonaqueous electrolytes, boast high energy densities, positioning them as preferred power storage solutions for diverse applications such as vehicles, mobile devices, and energy storage systems. However, the heightened energy density in these batteries poses significant challenges in safe management, evidenced by an increase in reported explosions involving such devices. Consequently, there has been burgeoning interest in all-solid-state batteries due to their exceptional manufacturing safety, facilitated by non-flammable solid electrolytes. Research predominantly centers on sulfide-based and oxide-based solid electrolytes. Sulfide-based variants exhibit comparable plasticity and Li$^+$ conductivity to conventional non-aqueous electrolytes. On the other hand, they lack water resistance and may react with ambient moisture to generate hydrogen sulfide, necessitating stringent moisture management protocols surpassing the dew point of –60 °C. Conversely, oxide-based solid electrolytes are more manageable and safer in atmospheric conditions. However, challenges arise due to their lower ionic conductivity and heightened

interface resistance with active materials, aggravated during the sintering process by potential side reactions.

Our prior investigations primarily focused on oxide-based solid electrolytes, specifically sintered multilayer oxide-based all-solid-state batteries utilizing the Na superionic conductor (NASICON)-type solid electrolyte $Li_{1.5}Al_{0.5}Ge_{1.5}(PO_4)_3$ (LAGP).[23] These batteries leverage lithium cobalt pyrophosphate $Li_2CoP_2O_7$ (LCPO) as the cathode material, operable at a high voltage of 5 V vs. Li^+/Li.[34] Notably, LCPO's oxidative decomposition potential in organic liquid-based batteries restricts its use; however, its compatibility with LAGP in an all-solid-state battery circumvents this issue, benefiting from LAGP's resistance to oxidative decomposition at high voltages. Consequently, our all-solid-state battery employing LCPO and LAGP facilitates efficient charge/discharge operations.[21] Conversely, the anode material utilized in our all-solid-state battery comprises anatase-type TiO_2, operational within a voltage range of 1.7 to 1.9 V vs. Li^+/Li. However, anatase-type TiO_2 may react during the sintering process with LAGP because the anatase-type TiO_2 crystal structure is unstable at over 800 °C. Anatase-type TiO_2 often transitions to rutile-type TiO_2 at temperatures ranging from 800 to 1000 °C, adding complexity during cell design. Moreover, considering the potential production of $Li_{1.4}Al_{0.4}Ti_{1.6}(PO_4)_3$ (LATP) through elemental substitution of Ti in Ge and TiO_2 in LAGP, a challenge emerges if both anatase-

type TiO_2 and LATP function as active materials for the anode at 2.5 V vs. Li^+/Li,[35] impacting

long-term charge/discharge cycles and cell stability. Therefore, the active material for the

sintered all-solid-state battery must have a stable structure without reacting with LAGP. The

cell design would be significantly difficult if both anatase-type TiO_2 and LATP act as active

materials for the anode material in an all-solid-state battery. Long-term charge/discharge

cycle tests might anticipate a shift in the charge/discharge depth between the cathode and

anode electrodes. Moreover, controlling unexpected charge/discharge behavior of LATP

induced during the sintering process poses a significant challenge. Hence, it become crucial

for the active materials in sintered all-solid-state batteries to maintain a stable structure,

preventing any reactivity with LAGP.

The thermodynamic strength of the rutile-type TiO_2 crystal structure surpasses that of

anatase-type TiO_2. Consequently, rutile-type TiO_2 is anticipated to maintain its crystalline

structure when sintered with LAGP. In this study, we fabricated sintered multilayer oxide-

based all-solid-state batteries utilizing rutile-type TiO_2 as the anode material and conducted

comparative analyses of their charge/discharge performances against those employing

anatase-type TiO_2. Additionally, we investigated the charge/discharge behavior of rutile-type

TiO_2 through Raman mapping analysis of the anode electrode layer in an all-solid-state

battery. Our focus primarily centered on understanding the correlation between

charge/discharge properties and capacity.

2.2 Experimental

In this study, anode materials comprised anatase-type TiO_2 (Sakai Chemical Industry Co., Ltd.) and crystalline rutile-type TiO_2 (Sakai Chemical Industry Co., Ltd.) as illustrated in Figures 2-1 (a) and (b).[36] The cathode material LCPO was synthesized through a solid-phase reaction.[22] Additionally, the solid electrolyte used was amorphous LAGP, synthesized via the melt-quenching method, with particle sizes ranging from 0.2 to 1 μm.[23] During the sintering process at 600 °C, the amorphous LAGP transformed into the crystalline phase $Li_{1.5}Al_{0.5}Ge_{1.5}(PO_4)_3$. The resulting crystalline LAGP exhibited an ionic conductivity of 2.0×10^{-5} S cm^{-1} at 25 °C, with an activation energy of 33.9 kJ mol^{-1} for Li$^+$ transport.
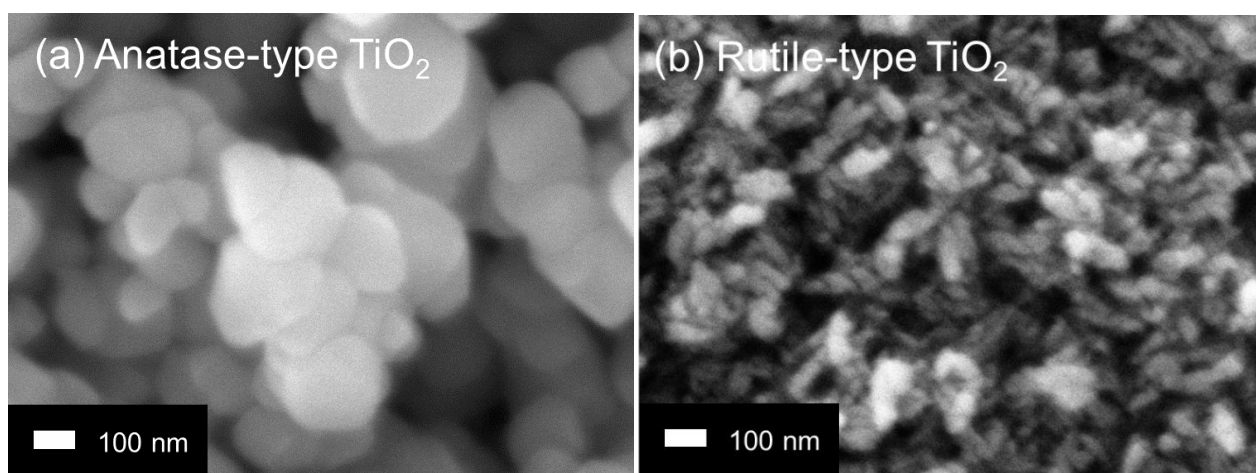

Figure 2-1. SEM Image (a) Anatase-type TiO_2 and (b) Rutile-type TiO_2

The crystal structures were determined using X-ray Diffraction (XRD) with a CuKα tube sphere as the source (XRD, SmartLab, Rigaku Corp.). The active material and solid electrolyte were characterized as follows: anatase-type TiO_2 features a tetragonal crystal structure (ICSD No. 154604, space group I41/amd), while rutile-type TiO_2 displays a tetragonal crystal structure (ICSD No. 202241, space group P42/mnm). LCPO exhibited a matching monoclinic peak pattern (ICSD No. 261899, space group P21/a), and LAGP corresponded to the peak pattern of the triclinic crystal (ICSD No. 69763, space group R-3c), reminiscent of $LiGe_2(PO_4)_3$ of NASICON. Particle size analysis was conducted using field-emission scanning electron microscopy (FE-SEM; JSM-IT700HR, JEOL Ltd.).

Electrode pellets for non-aqueous electrolyte cells were prepared by combining active materials, Acetylene Black (AB HS-100, Denka), and polyethylene terephthalate (PTFE, Aldrich) in a weight ratio of 25:60:15 wt%. These pellets were compressed into 8 mm diameter pellets using a press machine under a pressure of 15 kN, reaching an electrode thickness of 500 μm and a density of 1.0 g cm^{-2}. The electrochemical measuring cell designed for non-aqueous electrolytes was internally manufactured, capable of applying 0.7 kgf pressure. The non-aqueous electrolyte employed was EC/EMC (30:70 vol.%) (Tomiyama Pure Chemical Industries, Ltd.) containing 1 mol L^{-1} LiPF$_6$ as a solid electrolyte. A 20-μm-thick copper foil (Furukawa Electric Co., Ltd.) served as the collecting foil on the anode side,

where a 750 μm thickness lithium (Li) metal foil (Honjo Metal Co., Ltd.) was crimped onto the copper foil. Charging was executed with a constant current (CC) of 3.0 V vs. Li$^+$/Li endpoint, while discharge took place at 1.25 V vs. Li$^+$/Li endpoint, maintaining a temperature of 25 °C and a current density of 335 mA h g^{-1}, equivalent to 1 C rate. For measurements involving anatase-type TiO$_2$, discharge termination included a capacity termination condition of 100 mA h g^{-1}.

The thermal stability assessment of TiO$_2$, conducted through its mixing with a solid electrolyte and subsequent sintering, involved operating at 0.1 C rate for 10 cycles. Impedance measurements were performed using Solartron 1287A as the potentiostat and Solartron 1255B as the frequency response analyzer (Solartron Analytical). These measurements were carried out within a frequency range of 1 MHz−0.1 Hz, applying an amplitude of 5 mV (Figure 2-2).
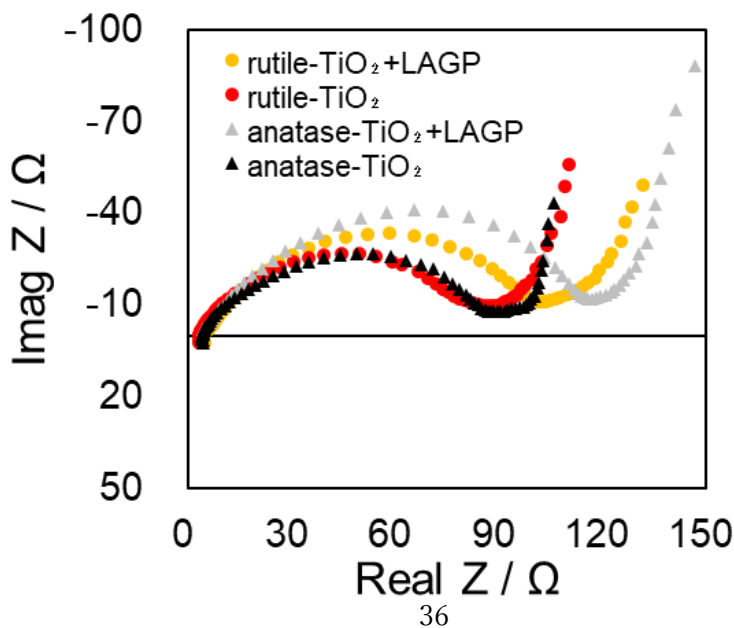
Figure 2-2. Impedance data of anatase-type TiO_2, after sintered anatase-type TiO_2 + amorphous LAGP, rutile-type TiO_2, and after sintered rutile-type TiO_2 + amorphous LAGP.

The all-solid-state battery developed in this study features a layered construction similar to a multilayer ceramic capacitor.[37,38] To fabricate the electrolyte green sheet, a mixture comprising 40 wt% LAGP amorphous powder, 30 wt% PVDF binder, and 30 wt% anhydrous alcohol (ethanol) as the solvent was ball-milled into a paste for 20 hours. After defoaming in a vacuum, this paste was doctor-blade coated onto a polyethylene terephthalate (PET) film, forming one layer of the electrolyte material. To reach a 20 μm thickness, multiple coated sheets were stacked, repeating the coating process until the desired thickness was achieved. The stacked layers were press-bonded and cut to the specified dimensions to form the electrolyte layer sheet. For the active material pastes, LCPO served as the cathode material, while TiO_2 was used for the anode electrode. A paste was prepared by mixing amorphous LAGP powder, acrylic resin binder, vapor-grown carbon fiber (VGCF, Resonac) as a carbon-based conductivity additive, and ethanol as the solvent. These pastes, adjusted to 50 μm thickness, were screen-printed onto the green sheet of the solid electrolyte, ensuring an equal amount of active material for both the cathode and anode layers. After coating, the paste was dried at 100 °C for 30 minutes. The LCPO and TiO_2 quantities in the cathode and

anode layers maintained an identical ratio. The green sheets, printed with cathode and anode electrodes, were alternately stacked, forming green chips in cuboid shapes. Following the removal of organic components from these green chips, the all-solid-state battery underwent sintering at 600 °C in a nitrogen atmosphere. Sintering process, the solid electrolyte measured between 6 and 9 μm in thickness, while the electrode thickness ranged between 15 and 25 μm. The electrode density for both cathode and anode electrodes was 0.3 g cm^{-2}.

In this experiment, the charge/discharge capacity of the all-solid-state battery was limited by the cathode material, LCPO. During charging, Li migrated from the cathode to the anode, with the reverse occurring during discharge. To fabricate the cells, the quantity of cathode material was adjusted to ensure the anode material reached a charge state of 20%. This specific charge depth corresponds to 120 μA h (70 mA h g^{-1}). Initially, the charge/discharge current was set at 1.6 μA mm^{-2} for cycles 1 to 10, employing a constant current (CC) of 3.6 V for charging and discharging at 0 V. Subsequently, the charge/discharge current was incrementally raised to 3.2, 6.4, 12.8, and 25.6 μA mm^{-2} every 10 cycles to evaluate the charge/discharge rate characteristics. Between cycles 51 and 55, the current value reverted to 1.6 μA mm^{-2} to further investigate charge/discharge rate properties.

The cross-sectional layers of the all-solid-state batteries were processed using a cross-sectional polisher device (IB-19510-CP, JEOL Ltd.). For spectroscopic analysis, a

microscopic laser Raman spectrometer (LabRAM HR Evolution VIS-NIR, HORIBA, Ltd.) was employed to analyze the Raman spectrum, specifically to observe the rutile-type TiO_2 within the anode layer of the batteries. Raman measurements were conducted at room temperature both before and after the charge/discharge process. The charging process involved a constant current/constant voltage (CCCV) of 3 V and a current density of 16 μA mm^{-2}, halted upon reaching a charge capacity of 130 μA h. Raman measurements were taken during a 40 minutes pause following the charging process. Subsequently, discharge was performed at a CC 0 V termination and a current density of 1.6 μA mm^{-2}. Further Raman measurements were conducted during 40 minutes pause after the discharge process. The Raman spectra were obtained within the 320–540 cm^{-1} range using a laser with a 457 nm wavelength, with an acquisition time of 1 second for each measurement point.

2.3 Results and Discussion

Initially, the charge/discharge behavior was studied to investigate the rate characteristics of a non-aqueous electrolyte cell using Li metal as the anode with rutile-type TiO_2 (Figure 2-3 (a)). It is known that rutile-type TiO_2 forms an inert Li phase (irregular monoclinic α-NaFeO$_2$ type Li$_x$TiO$_2$) around 1.1 V vs. Li$^+$/Li, leading to irreversible capacity.[39] Hence, the discharge cutoff voltage was restricted to 1.25 V vs. Li$^+$/Li to prevent

the formation of this irreversible phase. In conducting the charge/discharge test with limited

capacity, Li storage ceased near 1.25 V vs. Li$^+$/Li to prevent the formation of the irreversible

phase by regulating the amount of Li insertion and altering the Li desorption reaction.[40] Figure

2-3 (b) illustrates the charge/discharge behavior of the anatase-type TiO$_2$. In Figure 2-3 (c),

the transition of discharge capacity at varying charge/discharge rates is depicted. Anatase-

type TiO$_2$ exhibited a significant decrease in charging capacity, reaching a terminal voltage

of 1.25 V vs. Li$^+$/Li with an increase in the discharge rate. Conversely, rutile-type TiO$_2$
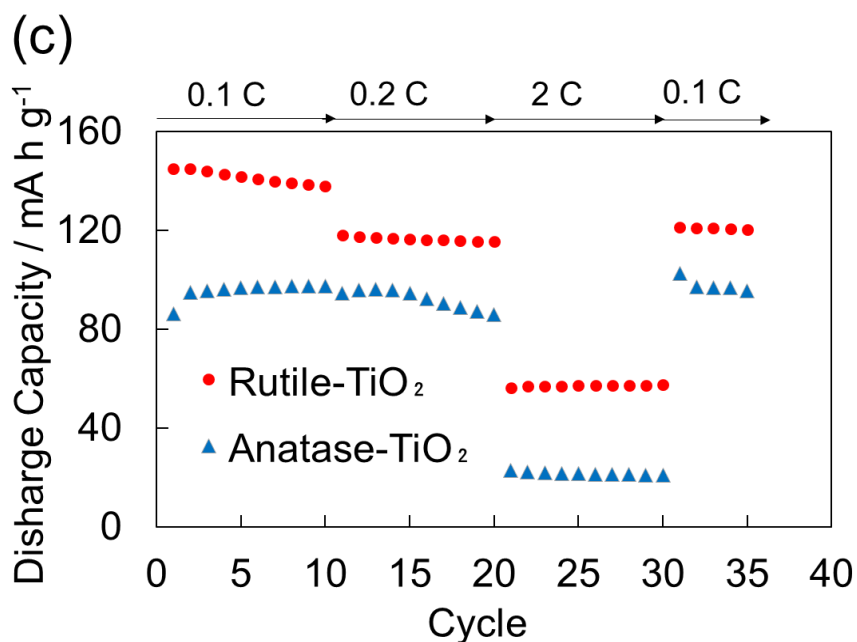
demonstrated a more favorable rate response.

(c)
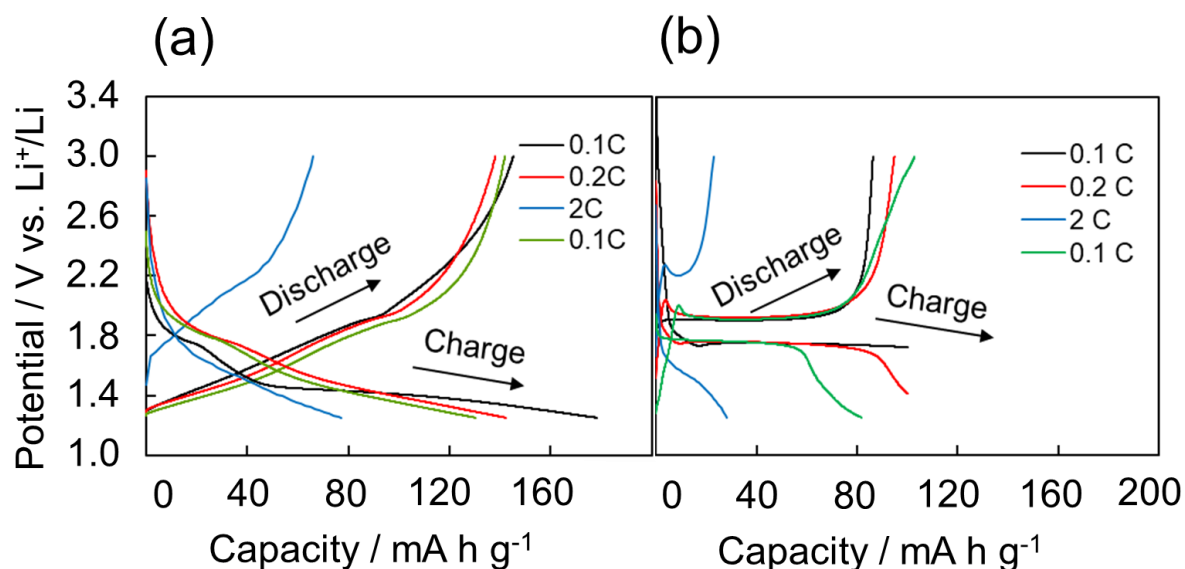
Figure 2-3. Charge/discharge curves at a current density of 33.5 mA g^{-1} (0.1 C) between 0.1 and 2 C for the (a) Rutile-type TiO$_2$ electrode, (b) Anatase-type TiO$_2$ electrode, and (c) Rate capabilities of rutile- and anatase-type TiO$_2$.

Subsequently, the thermal stability of TiO$_2$ was assessed upon its combination with a solid electrolyte and subsequent sintering. Upon mixing the TiO$_2$ anode material and the amorphous solid electrolyte LAGP at a 1:1 weight ratio, an electrode coating was generated using powder sintered in a nitrogen atmosphere at 600 °C. Subsequently, a charge/discharge test was conducted on the non-aqueous electrolyte cell. Figure 2-4 (a) illustrates the charge/discharge behavior of cells utilizing anatase-type TiO$_2$. The rut-type TiO$_2$ cell displayed a plateau in the charge/discharge curve ranging between 1.7 and 1.9 V vs. Li$^+$/Li.

41

The behavior observed in the anatase-type TiO_2 involves Li insertion, with the charge/discharge transitioning from the open-circuit voltage to 1.7 V vs. Li^+/Li. This phase is succeeded by a two-phase coexistence state between TiO_2 and tetragonal $LiTiO_2$, clearly demonstrated by a distinct flat plateau. The discharge cutoff voltage for the cell utilizing rutile-type TiO_2 was set at 1.25 V vs. Li^+/Li (Figure 2-4 (b)). Rutile-type TiO_2 demonstrated smooth shoulder curves within the range of 1.25 to 2 V vs. Li^+/Li. In the charge/discharge behavior of rutile-type TiO_2, the Li diffusion path predominantly occurs along the c-axis direction. Due to the low electron conductivity of TiO_2, the charge/discharge curve indicate as a gentle shoulder. In the case of sintered anode materials, the anatase-type TiO_2 sintered with amorphous LAGP exhibited a distinct shoulder in the charge/discharge curves, observable between 2 and 2.5 V vs. Li^+/Li (Figure 2-4 (c)). Conversely, rutile-type TiO_2, even when sintered with amorphous LAGP, showed minimal change in the charge/discharge behavior at 2.5 V vs. Li^+/Li (Figure 2-4 (d)). These observations suggest a potential alteration in the grain boundary between the anode materials and LAGP electrolyte after sintering. The results indicate the superior thermal stability of rutile-type TiO_2 compared to anatase-type TiO_2.
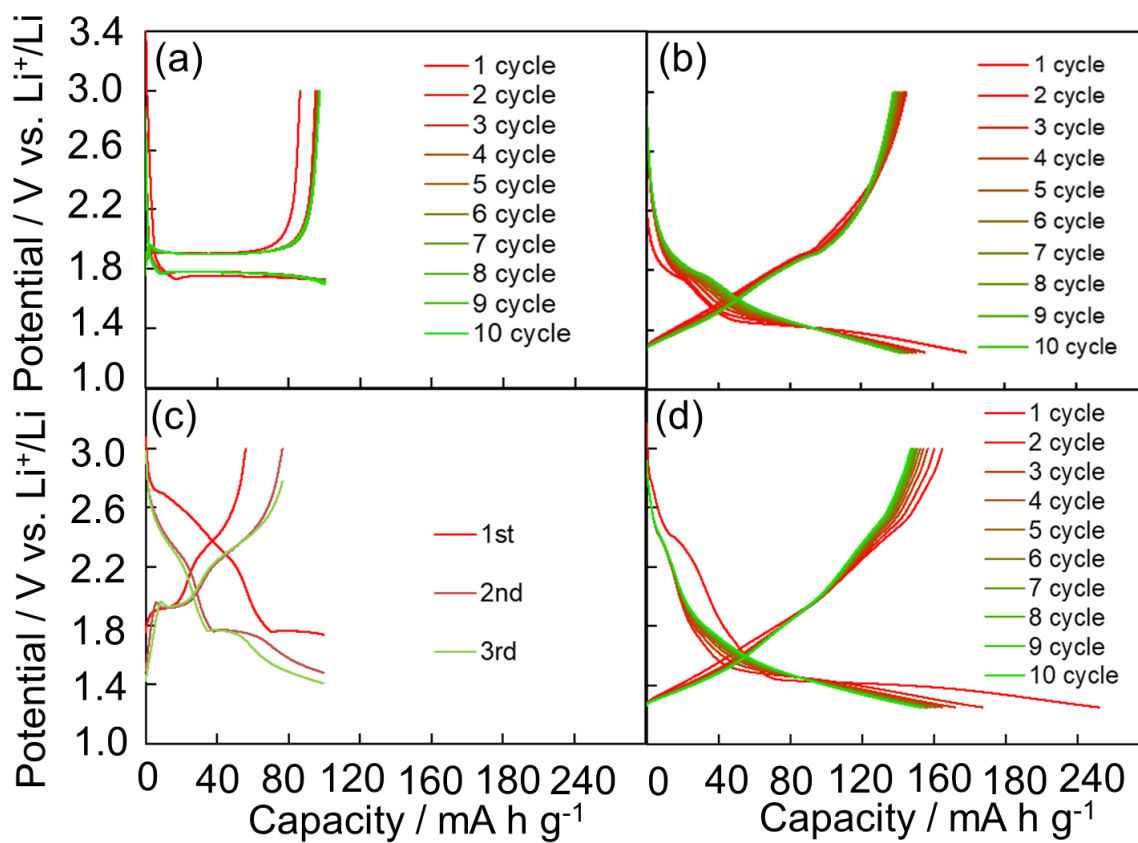
Figure. 2-4. Charge/discharge curves at a current density of 33.5 mA g^{-1} (0.1 C) during 10 cycles for the (a) Anatase-type TiO$_2$ electrode, (b) Rutile-type TiO$_2$ electrode, (c) Anatase-type TiO$_2$ electrode sintered with amorphous LAGP, and (d) Rutile-type TiO$_2$ electrode sintered with amorphous LAGP.

The XRD measurements conducted on the powder exhibited no detectable impurity phases, including LATP,[35] both before and after sintering of the anode material (Figures 2-5 (a), (b), (c), (d), (e), (f), (g), and (h)). The crystalline structure of rutile-type TiO$_2$ remained robust, showing no alterations in its charge/discharge behavior. However, after co-sintering

43

with amorphous LAGP, the first charge/discharge cycle exhibited an irreversible capacity for

rutile-type TiO_2. The initial charge/discharge efficiency was approximately 60%, improving

to over 90% during the second charge/discharge cycle. Prior studies have suggested that the

irreversible capacity of rutile-type TiO_2 can be attributed to the formation of a Li inert phase

(irregular monoclinic α-$NaFeO_2$ type Li_xTiO_2).[39] Consequently, it is assumed that during co-

sintering with amorphous LAGP solid electrolyte, Li was inserted into rutile-type TiO_2,

leading to the generation of an Li inert phase at the grain boundaries between TiO_2 and LAGP.
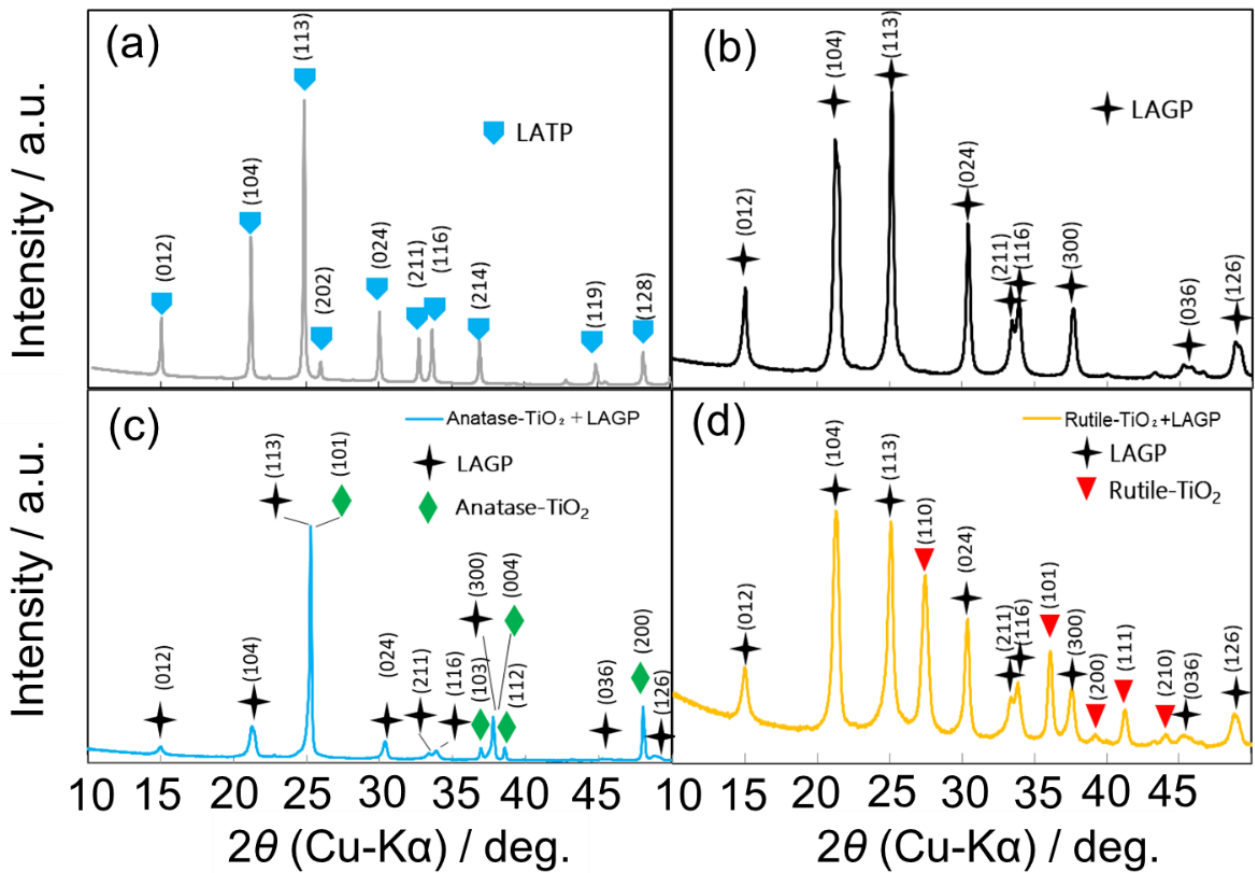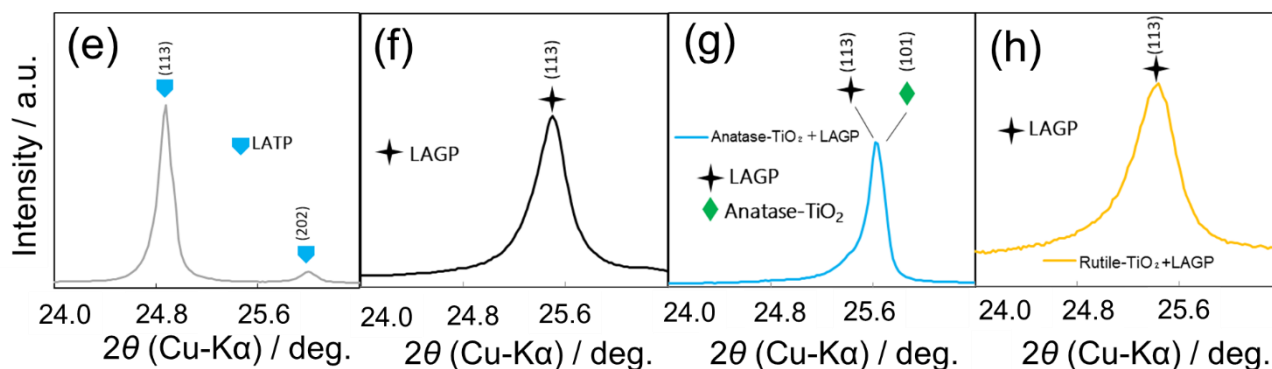
Figure 2-5. XRD peaks of (a) $Li_{1.4}Al_{0.4}Ti_{1.6}(PO_4)_3$ (LATP) , (b) $Li_{1.5}AL_{0.5}Ge_{1.5}(PO_4)_3$ (LAGP) ,

(c) after sintered anatase-type TiO_2 + amorphous LAGP, (d) after sintered rutile-type TiO_2 +

amorphous LAGP and expanded XRD peaks between 24°and 26.4° (e) $Li_{1.4}Al_{0.4}Ti_{1.6}(PO_4)_3$

(LATP) , (f) $Li_{1.5}AL_{0.5}Ge_{1.5}(PO_4)_3$ (LAGP) , (g) after sintered anatase-type TiO_2 + amorphous

LAGP, and (h) after sintered rutile-type TiO_2 + amorphous LAGP

The all-solid-state battery utilized both anatase- and rutile-type TiO_2 as anode

materials, paired with $Li_2CoP_2O_7$ as the cathode material. Figures 2-6 (a) and (b) depict the

behavior observed during the charge/discharge test conducted at a current value of 1.6 μA

mm^{-2}. Charging was stopped at a CC of 3.6 V, and discharge occurred at a CC of 0 V cutoff.

Notably, the all-solid-state batteries employing rutile-type TiO_2 were not charged beyond a

130 μA h capacity during the first and second cycles. In the initial charge/discharge cycle of

all-solid-state batteries employing anatase-type TiO_2, a distinct shoulder curve emerged

around 2.5 V, resembling the behavior seen in the non-aqueous electrolyte cell. Conversely,

no such 2.5 V shoulder curves were evident in all-solid-state batteries employing rutile-type

TiO_2. In terms of charge/discharge efficiency, an initial reversible capacity of approximately

80 % was observed, akin to the behavior observed in the non-aqueous electrolyte cell.

Subsequently, after the second cycle, a charge/discharge efficiency exceeding 90 % was

consistently achieved

Subsequently, to examine the input/output characteristics, the charge/discharge

current value was incremented from 1.6 μA mm^{-2} to 25.6 μA mm^{-2} every 10 cycles, as

illustrated in Figures 2-6 (c), (d), and (e). Rutile-type TiO_2 demonstrated superior

charge/discharge behavior compared to anatase-type TiO_2. Particularly at a current value of

25.6 μA mm^{-2}, the discharge capacity difference between rutile-type TiO_2 and anatase-type

TiO_2 was threefold, highlighting the excellent rate characteristics of rutile-type TiO_2 as an

anode material in all-solid-state batteries. Moreover, the irreversible capacity observed in the

solid-state battery was notably improved compared to that in the electrochemical measuring

cell, indicating potential involvement of the organic solvent in the electrochemical measuring
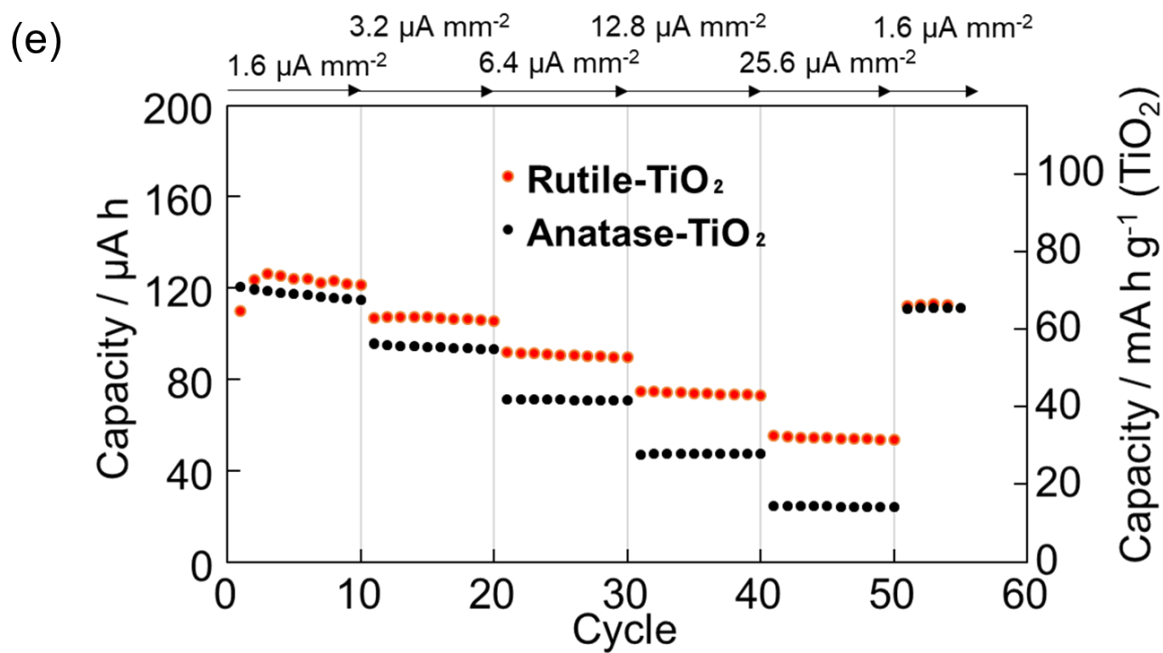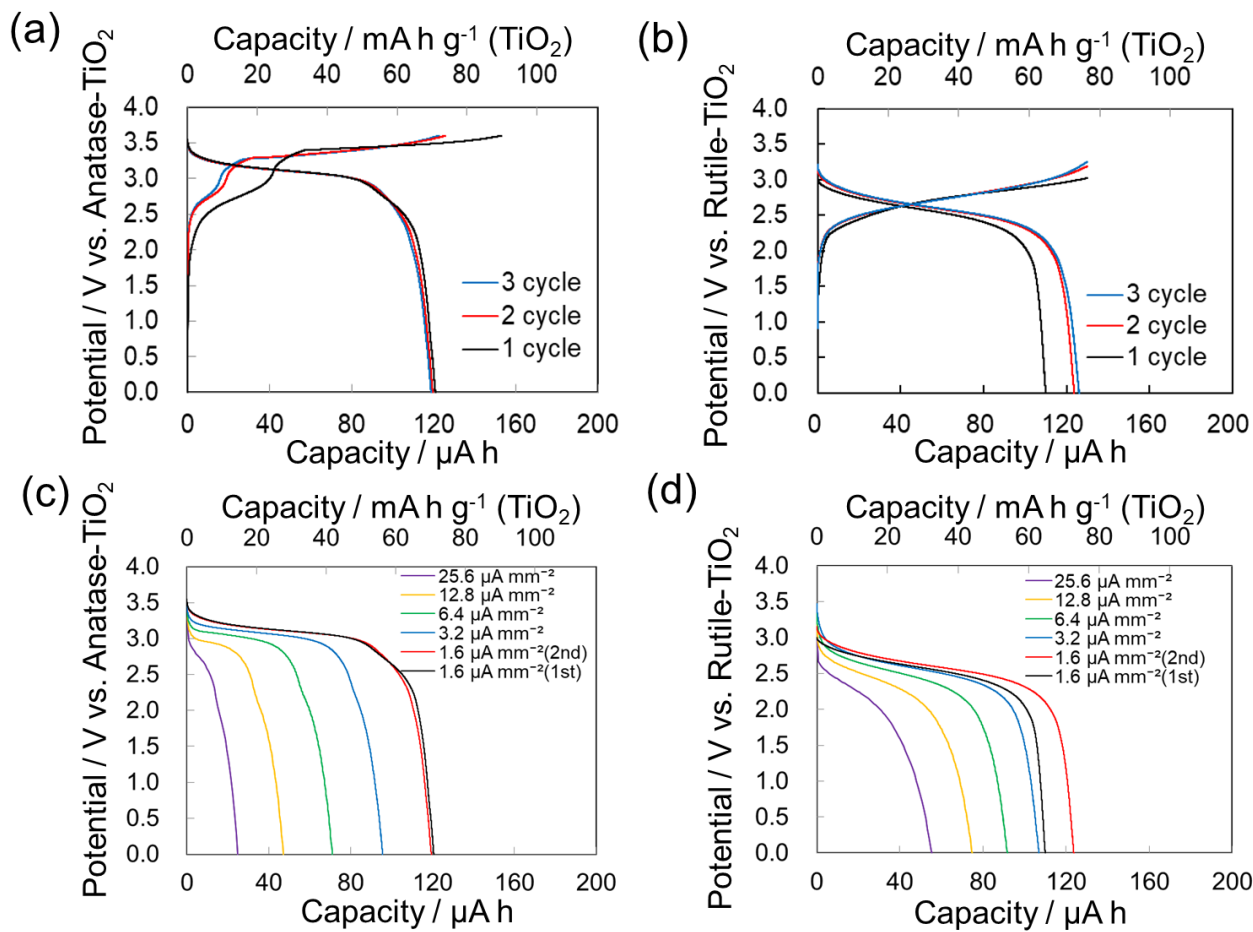
cell test.

(a), (b), (c), (d), (e)

Figure 2-6. Solid-state battery's charge/discharge curves at a current density of 1.6 μA mm^{-2} during three cycles for the (a) Anatase-type TiO_2 electrode and (b) Rutile-type TiO_2 electrode as anode material. Solid-state battery's discharge curves between 1.6 μA mm^{-2} and 25.6 μA mm^{-2} for the (c) Anatase-type TiO_2 electrode and (d) Rutile-type TiO_2 electrode as anode material. (e) Rate capabilities of the solid-state batteries between 1.6 μA mm^{-2} and 25.6 μA mm^{-2}.

The assessment of the all-solid-state battery using rutile-type TiO_2 exhibited superior rate characteristics compared to anatase-type TiO_2, with an average discharge voltage of 2.5 V. This distinction likely arises from the generation of an inert Li phase (irregular monoclinic α-NaFeO$_2$ type Li$_x$TiO$_2$), altering the charge/discharge behavior. To verify this assumption, an analysis of the atomic arrangement at the grain boundaries between LAGP and the crystalline phase of the anode material is crucial. The Raman mapping results obtained for the all-solid-state battery using rutile-type TiO_2 as the anode electrode, normalized by the Raman peak of 430 cm^{-1} of rutile-type TiO_2 before and after charge/discharge, are shown in Figures 2-7 (a), (b), (c), (d), and (e). Two cycles of charge/discharge were repeated under these conditions to capture the Raman shift of the rutile-type TiO_2 all-solid-state battery (Figures 2-7 (f) and (g)). Comparing the Raman shifts before and after charge/discharge,

focusing on the strongest peak intensity on the measurement plane, revealed a decrease in peak intensity and a shift towards the low wavenumber side during charging, followed by a return to the original position upon discharging. Christensen et al. previously demonstrated a decrease in Raman shift intensity due to Li insertion into rutile-type TiO_2 via a chemical approach,[39] which is consistent with our findings in this all-solid-state battery study. The observed shift in the Raman peak might also be attributed to stress distortion caused by expansion and contraction during charging and discharging. However, slight discrepancies between charge/discharge behaviors during the rate characteristic study and the Raman measurements might stem from variations in the cross-sectional processing of the all-solid-state battery. Therefore, the processing's impact on charge/discharge behavior warrants concurrent consideration.
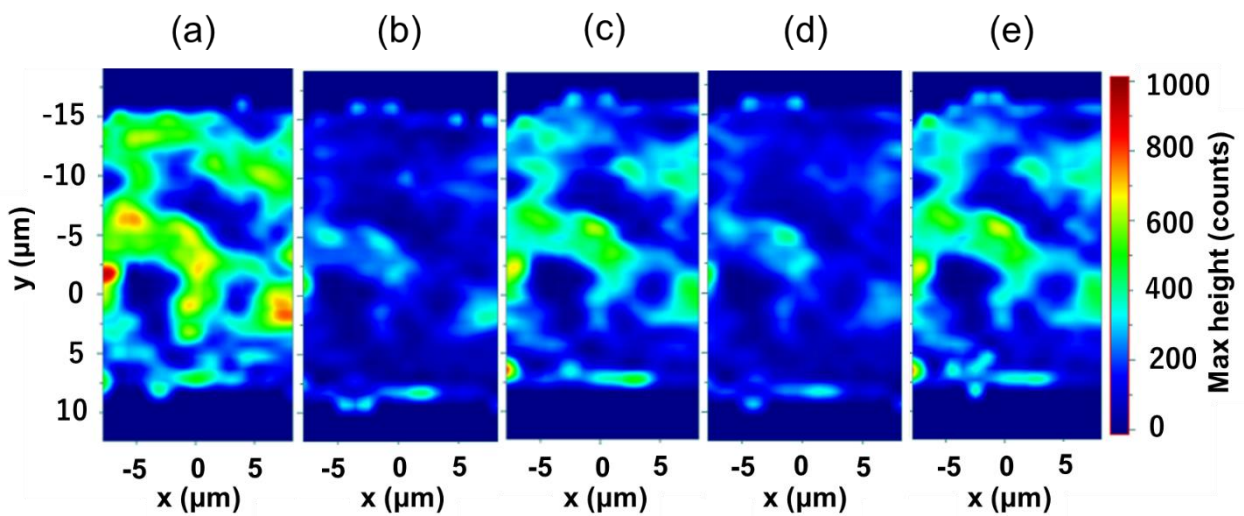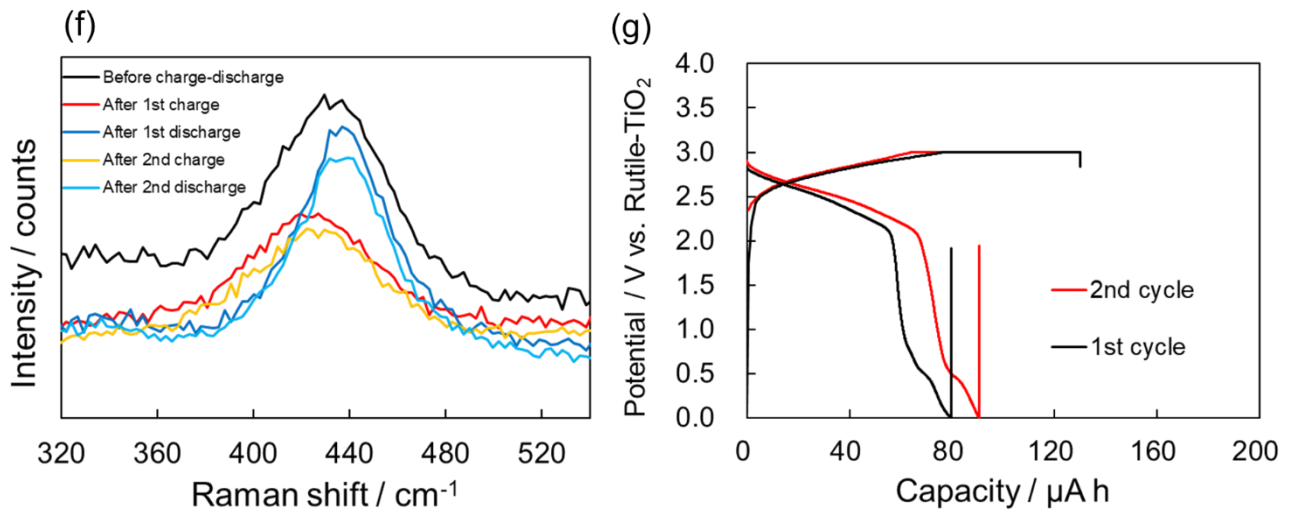
Figure 2-7. Solid state battery's Raman mapping results and Raman shift peak (430 cm^{-1}) for the (a) as-prepared battery, (b), (c) after first charge/discharge, and (d), (e) after second charge and discharge. (f) Raman shift peaks indicate the Raman wavenumber at each charge/discharge step. (g) charge/discharge curves during Raman measurements.

The investigation delved into the charge/discharge voltage phenomenon within anatase- and rutile-type TiO$_2$-based all-solid-state batteries, utilizing a Li metal half-cell. Specifically, a singular anode layer mimicking the all-solid-state battery composition underwent sintering, followed by gold deposition for current collection on one side, while Li metal, through a LiTFSA-containing polymer electrolyte, was placed on the opposite side, enclosed within a laminate to form a half-cell at 105 °C (Figure 2-8). The observed charge/discharge behavior in both cells indicated a reflection of the anode's operation in the

50

all-solid-state battery. The variation in operational voltage is postulated to stem from an alteration at the interface between the solid electrolyte LAGP and the anode material. Despite inconclusive evidence from XRD and Raman measurements regarding a distinct phase, the behavior shift is attributed to an interface layer of a few nanometers. Rutile-type TiO_2 demonstrates notable Li diffusivity within all-solid-state batteries, suggesting potential enhancements in battery performance. A comprehensive investigation is warranted to elucidate the causes behind the voltage behavior alteration and the Li diffusivity changes, furthering our understanding of rutile-type TiO_2 in all-solid-state battery applications.
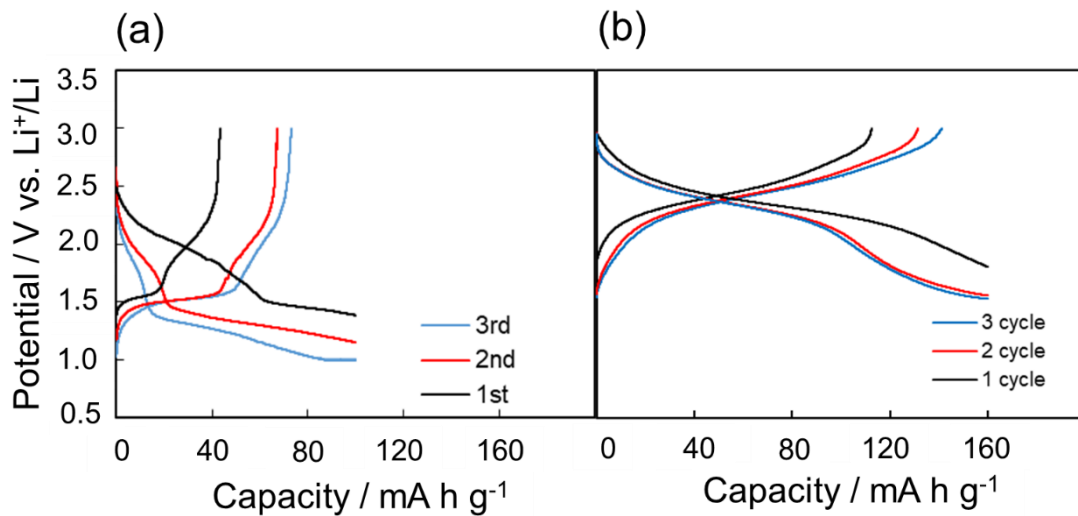

Figure 2-8. Charge/discharge curves of sintered anode layer half-cell which uses polymer electrolyte (LiTFSA) and Li metal as anode at 105 °C (a) Anatase-type TiO_2+LAGP and (b) Rutile-type TiO_2+LAGP.

2.4 Summary

Rutile-type TiO_2 emerged as a superior anode material, showing enhanced input/output characteristics compared to anatase-type TiO_2 across both electrolyte-based cells and all-solid-state batteries. While both anode materials exhibited charge/discharge voltage curve alterations in all-solid-state batteries, rutile-type TiO_2 maintained a notably higher Li diffusivity than anatase-type TiO_2. This discovery highlights the preservation of Li diffusivity within the bulk of the anode material even after co-sintering with a solid electrolyte, a pivotal finding in advancing battery design. Utilizing Raman spectroscopy, we successfully visualized the distribution of Li deinsertion reactions within rutile-type TiO_2, offering insights into the cross-section analysis of all-solid-state oxide batteries. This technique facilitated the visual comprehension of active material reaction distribution within the anode layer, a crucial aspect of all-solid-state battery performance assessment.

Further investigation into the solid-state interface is imperative to deepen our comprehension of reaction behaviors during charging and discharging. Analyzing elemental diffusion at the solid electrolyte-anode material interface through Transmission Electron Microscopy coupled with Electron Energy-Loss Spectroscopy (TEM-EELS), as well as exploring atomic arrangements using High Angle Annular Dark-Field Scanning Transmission Electron Microscopy (HAADF STEM) and annular bright-field (ABF) STEM,

will be pivotal in elucidating the grain boundaries between LAGP and the crystalline phase

of the anode material within all-solid-state batteries. These forthcoming endeavors aim to

provide comprehensive insights into the internal solid interfaces, propelling advancements in

all-solid-state battery technology.

Chapter 3

Electrochemical Anode Behavior of α-FeSi₂ co-Sintered with Solid Electrolyte

3.1 Introduction

Lithium secondary batteries boasting high energy densities are greatly sought after for applications in electric vehicles, mobile information terminals, and stationary energy storage systems. Solid-state batteries using oxide-based solid electrolytes are particularly appealing due to their safe handling under ambient conditions, eliminating risks associated with fire or toxic gas emissions. Nevertheless, these batteries present distinct challenges, such as the emergence of new reaction phases at the interface between the active material and the solid electrolyte during the battery fabrication's sintering process, as well as difficulties in achieving desired charge/discharge performance. Our focus has been on developing an all-solid-state battery utilizing $Li_{1.5}Al_{0.5}Ge_{1.5}(PO_4)_3$ (LAGP), a NASICON (Na Super Ionic Conductor)-type solid electrolyte, known for its oxide-based composition.[21] LAGP stands out due to its ability to be synthesized at around 650 °C, displaying a relatively high ionic conductivity of 1×10^{-5} S cm^{-1} at 25 °C, marking it as a promising solid electrolyte.[22] Furthermore, LAGP exhibits exceptional resistance to oxidation at high potentials and

remains stable at 5 V vs. Li$^+$/Li.[23] We're exploring the utilization of lithium cobalt

pyrophosphate Li$_2$CoP$_2$O$_7$ (LCPO) as a cathode material in this all-solid-state battery setup,

as its unconventional high potential could be integrated into the cell using LAGP as the solid

electrolyte and LCPO as the cathode material.[34] However, oxide-based solid electrolytes

inherently pose high interface resistance with the active material, necessitating optimization

of layer thicknesses akin to the structure of multilayer ceramic capacitors (MLCC).[37] Through

this approach, we've successfully manufactured a sintered multilayer oxide-based all-solid-

state battery, each layer measuring only a few micrometers thick, capable of consistent

charge/discharge at room temperature, a notable achievement.[33] In the pursuit of energy

density improvement, we've explored rutile-type TiO$_2$ as a potential anode material for all-

solid-state batteries employing oxide solid electrolytes. This material demonstrates a stable

crystal structure and excellent charge/discharge characteristics in nonaqueous electrolyte

cells.[16] In addition, it was reported rutile-type TiO$_2$ charge/discharge reversibly in non-

sintered all-solid-state battery.[41] When applied to sintered all-solid-state cells, no reaction

phase formed with the solid electrolyte, resulting in exceptional charge/discharge

characteristics.[13]

However, for further enhancement the energy density, an anode material operating at a lower

potential than LAGP's reduction would be preferable. In general, Li$_{1.5}$Al$_{0.5}$Ge$_{1.5}$(PO$_4$)$_3$

(LAGP) undergoes reduction decomposition reactions at potentials below 1.2 V vs. Li^+/Li.

Experimental evidence from a cell using a non-aqueous electrolyte revealed that during the

initial Li insertion, LAGP undergoes reduction and decomposition, resulting in the generation

of Ge. Subsequently, Ge forms an alloy with Li, completely forming LiGe, which undergoes

Li insertion and extraction reactions.[23]

In order to achieve a sustainable society, leveraging elements with high theoretical

capacity and abundant resources as active materials for batteries has become imperative.

Research focused on silicon anode materials is actively pursued, [42,43,44,45,46] and our attention

has been directed towards silicides due to their unique metal-like characteristics—displaying

ductility, malleability, and high electron conductivity.[47,48] Specifically, α-$FeSi_2$, with its

tetragonal crystal structure, finds applications across multiple fields, including solar cells,

optical sensors, thermoelectric conversion devices, thermal conductivity materials, and

semiconductor devices, owing to its semiconductor properties, optical attributes, and thermal

conductivity.[49] The adaptability of α-$FeSi_2$, customizable for specific applications, holds

particular significance in energy-related technologies.

In our prior investigation, we attained a reversible capacity of 630 mA h g^{-1} within

the voltage range of 0–2 V vs. Li^+/Li employing a nonaqueous electrolyte cell, showing the

remarkable attributes of $FeSi_2$.[50] Its effective integration into all-solid-state batteries could

potentially lead to a substantial increase in energy density. However, concerns arise regarding the reduction decomposition of NASICON-type solid electrolytes, resulting in a lack of reported studies on cell combinations involving silicon-based anode materials. Furthermore, there exists variation in the potential window values of solid electrolytes derived from theoretical calculations in different literature sources, contributing to a discrepancy observed in measured values across various experiments.[24]

Consequently, this investigation focused on determining the existence of reaction phases and assessing the electrochemical traits of a blend comprising amorphous LAGP and silicon anode material sintered at 600 °C in a nitrogen environment. The study involved several analyses, encompassing an examination of the reduction decomposition tendencies of LAGP within a solid-state cell using a sintered sheet, as well as the characterization of the compounds produced within the electrode throughout the charge/discharge cycles.

3.2 Experimental

The anode materials within the Si-based system encompassed Si, SiO, $NiSi_2$, and $FeSi_2$, each possessing a purity of 99.9% (sourced from Kojundo Chemical Laboratory Co., Ltd.). These materials exhibited a particle size of 1.0 μm ($D50$). Amorphous LAGP, identified

57

by its white particle appearance and boasting a 99.9 % purity, featured a particle size ($D50$) of 0.5 μm, acquired from Toshima Manufacturing Co., Ltd.

To assess the crystal structure, X-ray Diffraction (XRD) analysis utilized a CuKα tube as the source, implemented through the SmartLab XRD apparatus by Rigaku Corp. Raman spectroscopy, conducted using a micro-laser Raman spectrometer (LabRAM HR Evolution VIS-NIR, HORIBA, Ltd.), aimed to identify SiO and acquire the Raman spectrum of the Si phase present in $FeSi_2$. This measurement spanned the spectral range of 440–560 cm^{-1}, employing a 457 nm laser wavelength with an exposure time of 1 second per data point and an accumulation of four times.

The sintering experiment involved preparing a mixture of the anode material and amorphous LAGP in a mortar at a mass ratio of 50:50 wt%. The heating condition progressed at 100 °C h^{-1}, followed by sintering in a nitrogen atmosphere at 600 °C for 2 hours, with a cooling rate of -100 °C h^{-1}.

For the measurement of electronic conductivity, a potentiostat-galvanostat (SP-300, BioLogic) was employed. A press cell (KP-SolidCell, Hohsen Corp.) served as the powder-pressing fixture. The procedure involved placing the mixed powder (50 mg) into the pressure cell and applying a torque pressure of 20 N·m. Initial resistance values were derived from the current generated by applying voltages ranging from ±0.1 to 0.5 V, each maintained for 300

seconds, calculated using the formula $V=IR$. Subsequently, the electrical resistivity was determined from the obtained resistance values, considering the thickness and area of each sample. Finally, electronic conductivity was ascertained as the reciprocal of the electrical resistivity.

In the formulation of the sintered sheet, $FeSi_2$, amorphous LAGP, and vapor-grown carbon fiber (VGCF, Resonac) were utilized as conductive additives, ensuring the final solid content after sintering was $FeSi_2$:LAGP:VGCF = 30:60:10 wt%. For the paste preparation, a blend of $FeSi_2$, amorphous LAGP, and VGCF, mixed with polyvinylidene difluoride (PVDF) and anhydrous isopropanol in a ratio of 20:30:50 wt%, underwent ball milling for 20 hours, followed by vacuum degassing. Application of the paste onto a polyethylene terephthalate (PET) film using the doctor blade method was succeeded by solvent removal in a dryer operating at 150 ℃, yielding an unsintered, single-layer sheet termed a "green sheet."

To attain the desired electrolyte layer thickness, a specific number of green sheets from a single coating were press-laminated, resulting in a laminated green sheet measuring 300 μm in thickness. This laminated green sheet, sized at 20 × 20 mm, constituted the electrode green sheet. The sintering process, carried out in a nitrogen atmosphere, followed a heating rate of 100 ℃ h^{-1}, maintaining a temperature of 600 ℃ for 2 hours, succeeded by a

cooling rate of -100 °C h^{-1}. After sintering, the dimensions of the sintered sheet measured 17

$\times$ 17 mm with a thickness of 230 μm, and the FeSi$_2$ electrode density registered at 1.93 g cm^{-3}.

To assemble the solid-state evaluation cell, gold was sputter-deposited on one side of

the sintered sheet, serving as the current collector. Following a 12 hours drying period at

150 °C in a vacuum dryer within a glove box, a polymer electrolyte (lithium

bis(trifluoromethanesulfonyl)amide or LiTFSA from Osaka Soda Co., Ltd.) measuring 80 μm

in thickness was inserted between the sintered sheet and Li metal. The Li metal, cut into 22

mm squares and affixed to a copper foil, formed the counter electrode. These components—

sintered sheet, polymer electrolyte, and Li metal were enclosed within an aluminum

laminated film, creating the evaluation cell.

Charge/discharge procedures were conducted using charge/discharge equipment

(HJ1001SD8, Hokuto Denko Co., Ltd.) at a constant current value of 0.01 C rate, maintaining

a constant temperature of 105 °C. Charge involved Li insertion into the anode material, while

discharge involved Li removal from the material.

After the charge/discharge cycles, cell disassembly within the glove box preceded the

sintered sheet voltage confirmation using a handheld digital multimeter (KU-1133, Kaise

Corp.). Subsequent matching of dimensions to the measurement fixture ensured secure

installation for XRD measurements under controlled conditions, preventing exposure to air.

For comparative analysis, charge/discharge behaviors of the $FeSi_2$ electrode composite were investigated using a cell employing a nonaqueous electrolyte. The composite, comprising $FeSi_2$, acetylene black (AB Li-400, Denka), and polytetrafluoroethylene (PTFE, Aldrich) at a weight ratio of 25:60:15 wt%, was pressed into pellets of 8 mm diameter using press equipment at a pressure of 15 kN. This electrode exhibited a thickness of 400 μm and a density of 1.0 g cm^{-3}. Electrochemical measurements were conducted using a custom-made cell capable of applying a pressure of 0.7 kgf. The electrolyte utilized was 1 mol dm^{-3} (M) $LiPF_6$ dissolved in a mixture of ethylene carbonate (EC) and ethyl methyl carbonate (EMC) in a volume ratio of 30:70 from Tomiyama Pure Chemical Industries, Ltd. Charge/discharge procedures were performed at a current rate of 50 mA g^{-1} (0.12 C rate) for a total of ten cycles, with charge termination set at 0 V and discharge termination at 3 V. Controlled conditions at a temperature of 23 °C were maintained throughout the cycles.

3.3 Results and Discussion

The XRD measurements revealed crystalline Si in a cubic phase and SiO exhibiting a broad peak (Figures 3-1 (a) and (b)). Raman spectroscopy confirmed the presence of amorphous Si within amorphous SiO (Figure 3-2 (a)). $NiSi_2$ and $FeSi_2$ corresponded to their respective databases in the XRD patterns (Figures 3-1 (c) and (d)). $FeSi_2$ displayed XRD

peaks related to impurity phases of FeSi, and the Raman spectra showed partial presence of crystalline Si phases (Figure 3-2 (b)). It's notable that $FeSi_2$ exhibited insufficient formation of silicide phases, a point duly noted and considered in this study. Amorphous LAGP exhibited a broad peak and aligned with $LiGe_2(PO_4)_3$ of NASICON when sintered at 600 °C in a nitrogen atmosphere (Figure 3-1 (e))
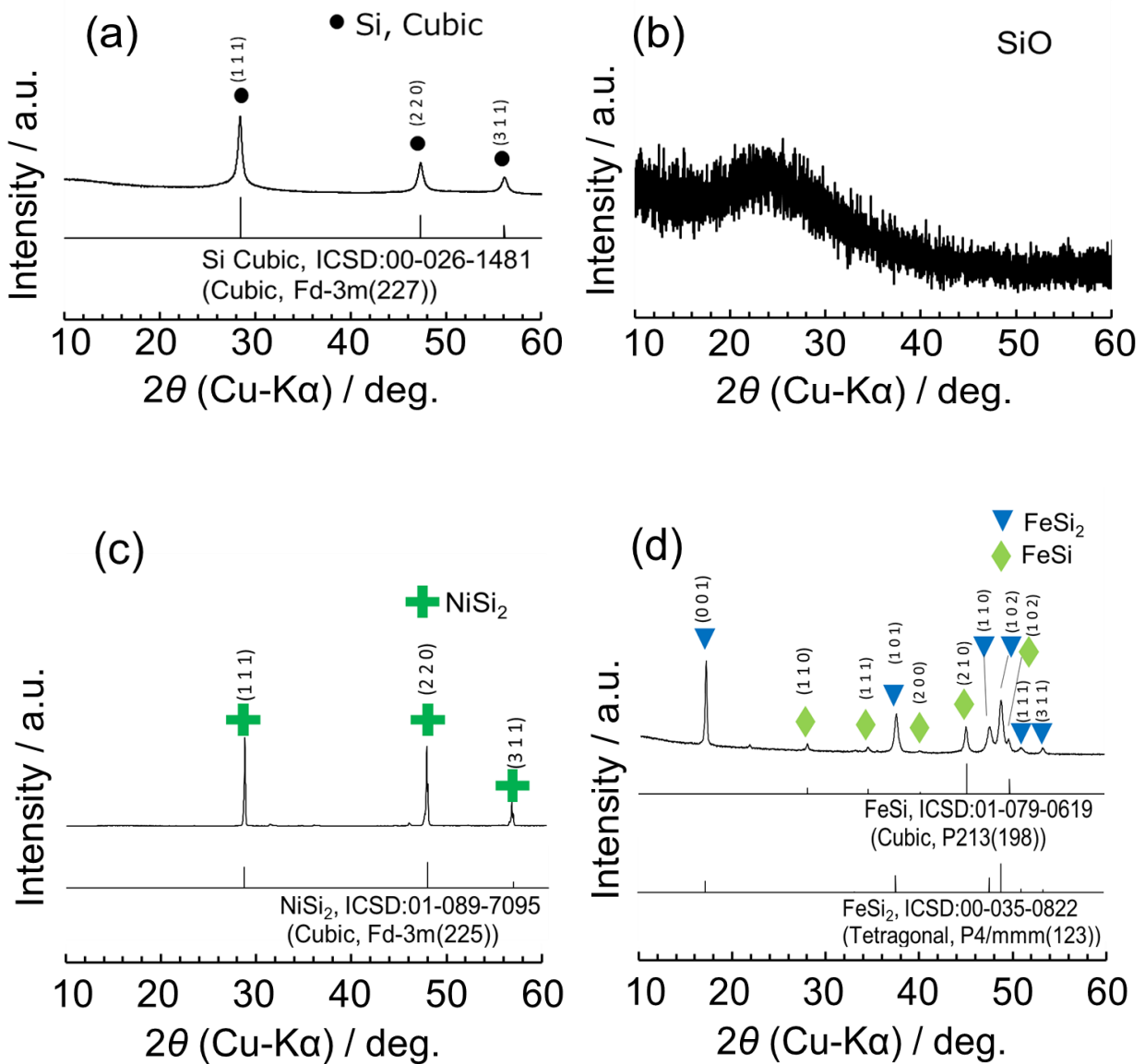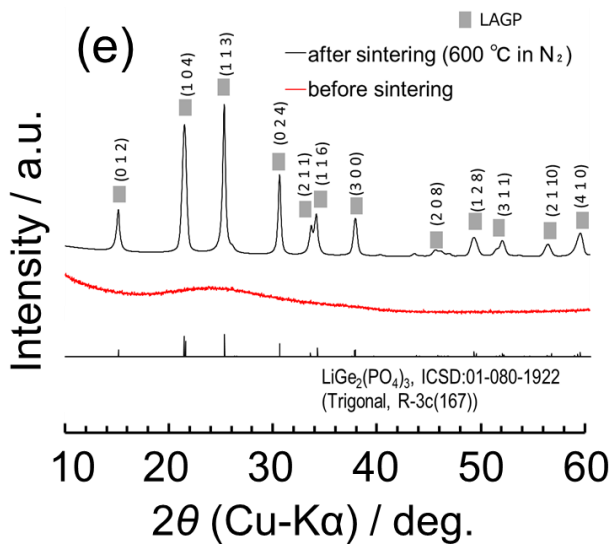
Figure 3-1. XRD patterns of (a) Si, (b) amorphous SiO, (c) NiSi$_2$, (d) FeSi$_2$, and (e) LAGP
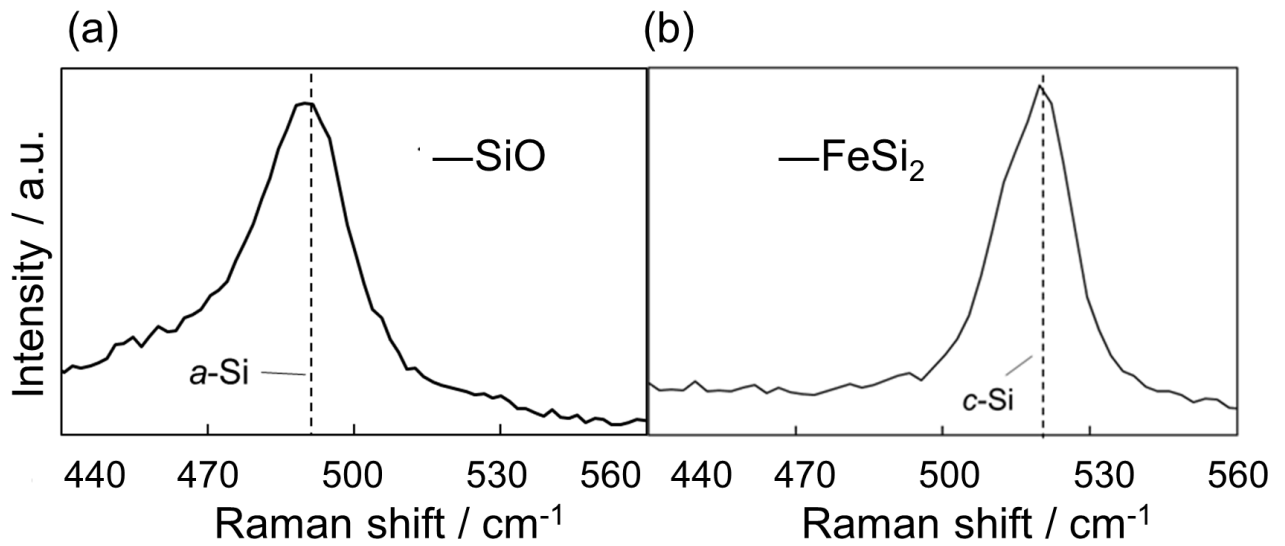
before /after sintering.

Figure 3-2. Raman spectra of (a) amorphous SiO and (b) FeSi$_2$.

Figure 3-3 presents XRD measurements subsequent to mixing amorphous LAGP and

powders of each anode material at a mass ratio of 50:50 wt% and sintering at 600 ℃ in a

nitrogen atmosphere. In the Si (cubic) sintering results (Figure 3-3 (a)), there was minimal

presence of peaks derived from the crystalline LAGP phase. Additionally, the emergence of

GeSi (cubic) and $LiAlP_2O_7$ confirmed the formation of reaction phases. Figure 3-3 (b)

indicated the formation of a crystalline LAGP phase alongside GeSi (cubic) and $LiAlP_2O_7$.

$NiSi_2$ (Figure 3-3 (c)) exhibited diffraction patterns of both LAGP and $NiSi_2$ (cubic),

accompanied by the formation of $LiAlP_2O_7$ as the reaction phase. Concerning $FeSi_2$

(tetragonal) (Figure 3-3 (d)), primary phases identified were LAGP and $FeSi_2$ (tetragonal),

with FeSi remaining as an impurity phase after sintering, while the formation of GeO_2

(tetragonal) was confirmed as the reaction phase.

These results suggest reactions between Si, SiO, and LAGP, resulting in the

appearance of GeSi upon sintering at 600 ℃. Notably, the GeSi peaks shifted approximately

0.4° towards the lower-angle side compared to the GeSi peak in the database, attributed to

the deviation in the substitution solid solution ratio of Ge and Si from 1:1. In the case of $NiSi_2$,

the intensity of the $LiAlP_2O_7$ peak surpassed those of Si and SiO, indicating a trend of further

$LiAlP_2O_7$ formation. For $FeSi_2$, the appearance of GeO_2 after co-sintering with LAGP was

observed. This phenomenon has been reported in studies on amorphous LAGP

crystallization.[22,26] We've previously confirmed GeO_2 formation at higher sintering temperatures of amorphous LAGP.[51] This occurrence is linked to the presence of amorphous GeO_2 within amorphous LAGP.

Amorphous LAGP is obtained by melting raw materials at 1300 °C, and it's presumed that a small amount of Li volatilizes during sintering. As GeO_2 has a melting point of 1100 °C, it's suggested that amorphous GeO_2 crystallized during co-sintering with $FeSi_2$ due to a deviation from the theoretical composition. This inference supports the notion that $FeSi_2$'s presence accelerates LAGP crystallization, causing GeO_2 formation. Moreover, in the presence of $NiSi_2$, GeO_2 crystallization is absent. Given $NiSi_2$'s identical crystal system (cubic) and space group (Fd-3m) to GeSi, it suggests that some GeSi forms in $NiSi_2$, precluding GeO_2 formation.
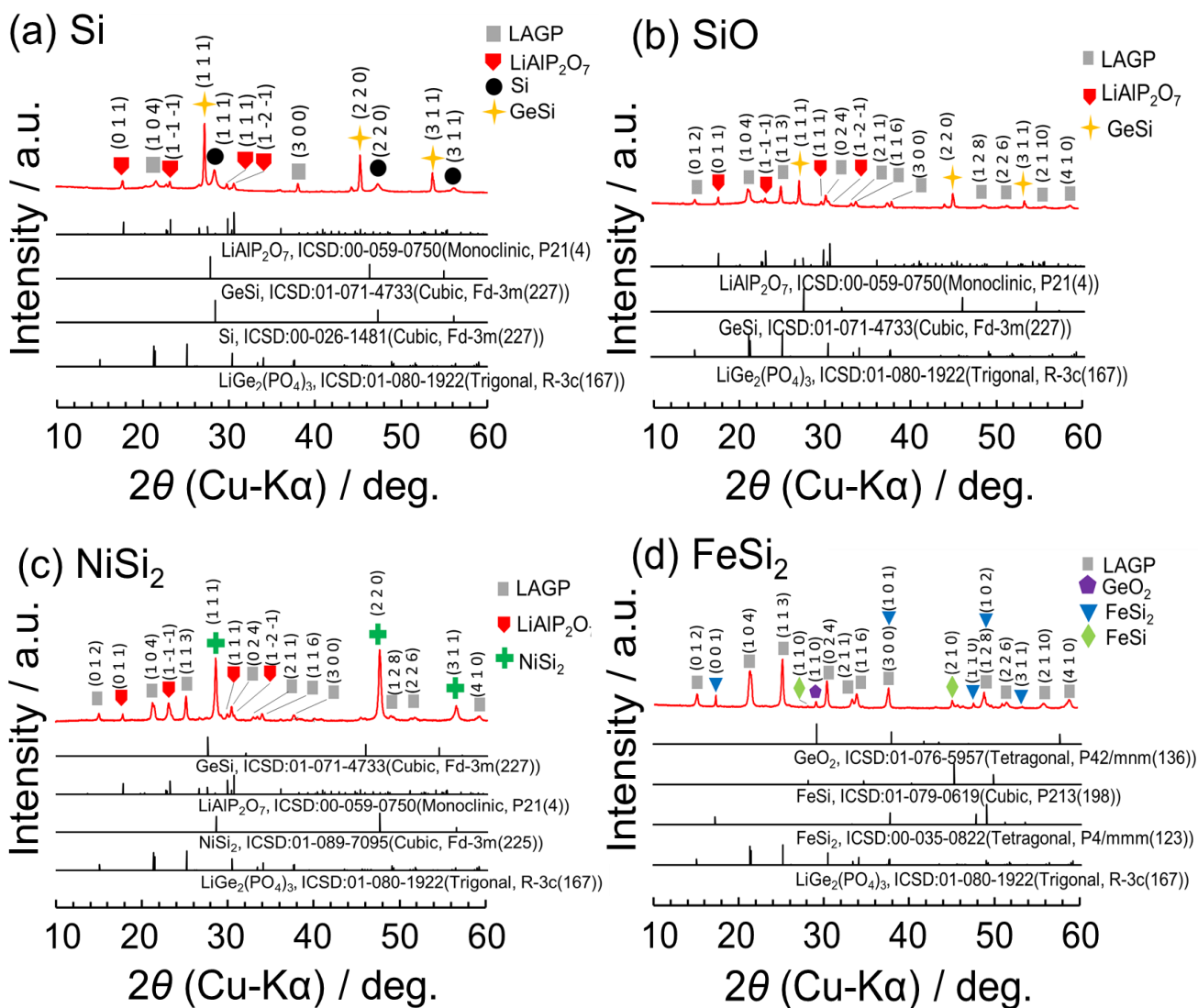
Figure 3-3. XRD patterns of a mixture of amorphous LAGP and (a) Si, (b) SiO, (c) NiSi$_2$, and

(d) FeSi$_2$ at a mass ratio of 50:50 (wt%) after sintering at 600 °C in a nitrogen atmosphere.

The reason for the subdued reaction phase observed in tetragonal crystal structures compared to other Si-based materials likely indicates in the structural attributes that contribute to suppressing reactions with amorphous LAGP. In prior work, rutile-type TiO_2, also exhibiting a tetragonal structure, was utilized in all-solid-state batteries, showing no observable reaction phase during sintering tests with amorphous LAGP.[33] This pattern suggests stability of materials with a tetragonal structure within amorphous LAGP, as also seen with GeO_2, which is tetragonal configuration. In the crystal system, LAGP's trigonal structure features crystal axis lengths of a = b = c, unequal crystal axis angles of $\alpha = \beta = \gamma \neq$ 90°, and a highly distorted framework. In contrast, the tetragonal structure displays crystal axis lengths of a = b $\neq$ c, with crystal axis angles of $\alpha = \beta = \gamma = 90°$, potentially contributing to maintaining stability within the trigonal structure. The impact of crystal systems on structure stability can be explained through the process of crystallization within amorphous LAGP, which moves from a metastable equilibrium state to a metastable crystalline phase and eventually to a stable crystalline phase. Ostwald's step rule, a crucial empirical concept in understanding crystallization processes, indicates that crystalline phases with higher thermodynamic Gibbs free energy tend to appear before those with lower free energy. Consequently, during the formation of the metastable phase of LAGP, the tetragonal phase maintains its structure within the metastable phase of LAGP because its Gibbs free energy is

higher than or equal to that of the LAGP metastable phase. However, further comprehensive

investigations are required, encompassing the homogeneity of the LAGP metastable phase

and lattice contraction during phase transitions, to fully understand the implications and

mechanisms of these structural interactions.

To verify the persistence of high electronic conductivity in silicides after sintering,

we examined the electronic conductivity of the powders before and after the sintering process.

Table 3-1 presents the obtained electronic conductivity values derived from the direct current

resistance of each powder. Single Si and SiO exhibited an electronic conductivity of

approximately 10^{-9} S cm^{-1}, indicating a lack of electronic conductivity. Conversely, NiSi$_2$

and FeSi$_2$ showed electronic conductivity within the range of $10^{-1} - 10^{-0}$ S cm^{-1}, comparable

to acetylene black (AB), a commonly used carbon-based conductive additive in cells utilizing

nonaqueous electrolytes. These values remained consistent even after sintering in a nitrogen

atmosphere at 600 °C. However, when the powders underwent co-sintering with amorphous

LAGP, there was a notable decrease in electronic conductivity. NiSi$_2$ displayed a significant

decrease to 10^{-9} S cm^{-1}, while FeSi$_2$ exhibited 10^{-3} S cm^{-1}. These alterations correlated with

the presence or absence of reaction phases following sintering with LAGP, as evidenced by

the XRD results. In the case of NiSi$_2$, the formation of an insulating LiAlP$_2$O$_7$ phase was

observed,[52] leading to the drastic reduction in electronic conductivity of the sintered powder

with LAGP. Conversely, FeSi$_2$ maintained its crystal structure stability even after co-sintering

with LAGP, enabling it to retain a high level of electronic conductivity.

Table 3-1 Electronic conductivity of each active material powder under various conditions.

Sample	Sintering process			Weight ratio			Electronic conductivity
	Atmosphere	Temp./℃	FeSi$_2$ /wt%	NiSi$_2$ /wt%	Amorphous LAGP/wt%		at 25 ℃ / S cm^{-1}
Acetylene Black	—	—	—	—	—		4.2×10^{-0}
Si	—	—	—	—	—		3.1×10^{-9}
SiO(amorphous)	—	—	—	—	—		4.4×10^{-9}
NiSi$_2$	—	—	—	—	—		1.2×10^{-0}
NiSi$_2$	N$_2$	600	100	—	—		1.1×10^{-0}
NiSi$_2$+LAGP	N$_2$	600	—	50	50		1.0×10^{-9}
FeSi$_2$	—	—	—	—	—		3.0×10^{-1}
FeSi$_2$	N$_2$	600	100	—	—		2.1×10^{-1}
FeSi$_2$+LAGP	N$_2$	600	50	—	50		9.0×10^{-3}

FeSi$_2$ demonstrated a preserved crystal structure and electronic conductivity

following co-sintering with amorphous LAGP. Consequently, an evaluation cell employing

FeSi$_2$ was assembled, and its charge/discharge behavior was analyzed. The morphology of

the sheet's cross-section after sintering was verified through scanning electron microscope

(SEM) observation (Figure 3-4), affirming the formation of a compact and dense sintered
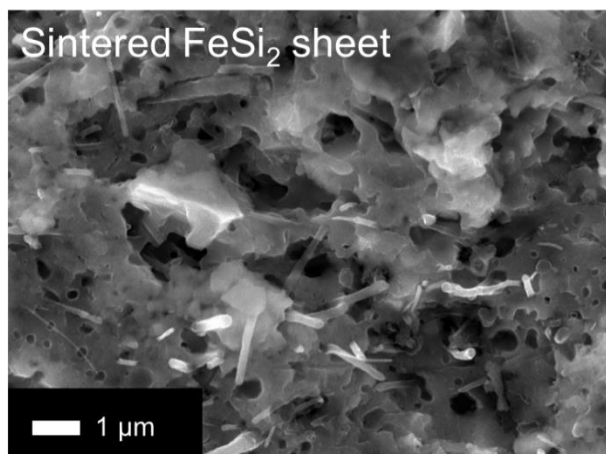
sheet.

Figure 3-4. The sheet's cross section appearance of SEM observation.

Figure 3-5 shows the charge/discharge curves acquired at 105 ℃ under various charge/discharge cutoff conditions. Charging denotes the process when Li is inserted, while discharging refers to Li removal. Consistently, the discharge termination voltage across all assessed cells was set at 3 V vs. Li$^+$/Li. In Figure 3-5 (a), the initial charging process ceased upon reaching the maximum capacity of 630 mA h g^{-1} (Li$_{2.6}$FeSi$_2$), based on FeSi$_2$'s reversible capacity in cells utilizing a nonaqueous electrolyte. Figures 3-5 (b) and (c) illustrate charge/discharge curves after consecutive charge/discharge tests, up to the third cycle. The distinction shows in Figure 3-5 (b), where charging extended to 0 V vs. Li$^+$/Li in the first cycle, whereas in Figure 3-5 (c), charging stopped at a charge capacity of 855 mA h g^{-1}, equivalent to Li$_{3.6}$FeSi$_2$, surpassing the maximum capacity, followed by discharging. Subsequent charging cycles involved charging until the charging voltage reached 0 V vs.

70

Li$^+$/Li. Following each condition, the evaluation cell underwent disassembly, and ex-situ

XRD measurements were conducted at specified points (II, III, and IV) corresponding to the
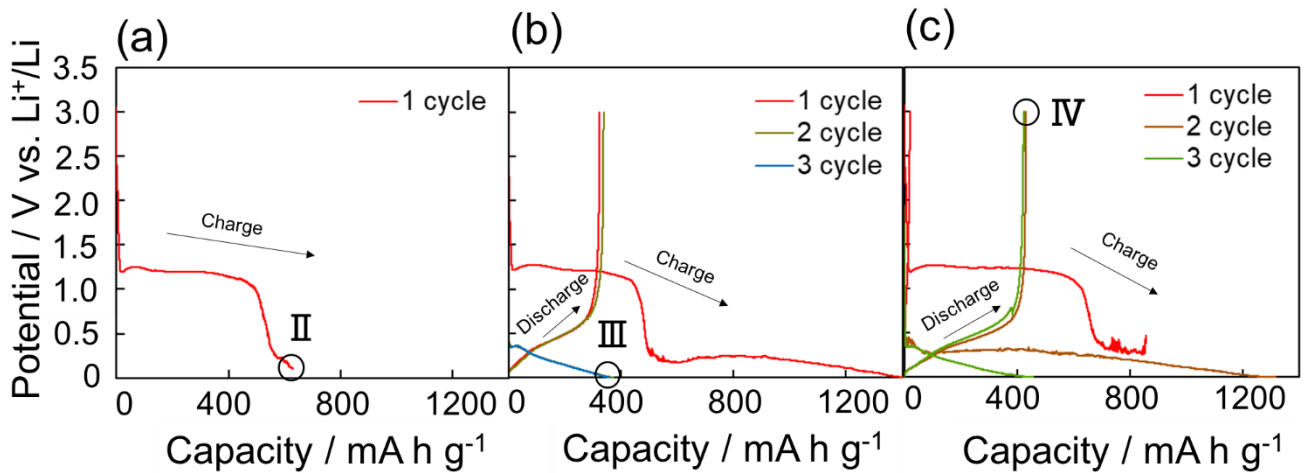
conclusion of each charge/discharge assessment.

Figure 3-5. Charge/discharge profiles of sintered sheet electrodes using FeSi$_2$. The

measurement was stopped after (a) the first charge process at 630 mA h g^{-1}, (b) the third

charge process at 0 V, and (c) the third discharge process at 3 V. (The circle in the figure

indicates the XRD measurement points after the cell disassembly).

During the initial charge, a consistent plateau region emerged at 1.25 V vs. Li$^+$/Li

across all conditions. Figure 3-5 (b) reveals an approximate discharge capacity of 400 mA h

g^{-1} upon charging to 0 V vs. Li$^+$/Li. Conversely, Figure 3-5 (c) indicates no observable

discharge reaction, even with charging surpassing the theoretical capacity of FeSi$_2$ after initial

charge. These observations suggest that the primary charging reaction occurs within the 0–1

71

V vs. Li$^+$/Li plateau region. The presence of the 1.25 V vs. Li$^+$/Li plateau during the initial

charge likely relates to the reduction decomposition of LAGP, as noted in prior study.[23]

Thus, an anticipation arose that subsequent charging might not yield the anticipated 0–1 V

Li$^+$/Li plateau and reversible charge/discharge behavior due to LAGP's reduction and

decomposition, consequently lacking a Li conductor. However, contrary to expectations, this

study observed charge/discharge behavior. These outcomes suggest that the reduction

decomposition product of LAGP might serve as a Li conductor in the solid-state cell,

facilitating the progression of charge/discharge reactions. Figure 3-6 shows the

charge/discharge outcomes for FeSi$_2$ in the cell utilizing a non-aqueous electrolyte. Notably,

distinct charge/discharge curves were observed between the evaluation cell and the cell

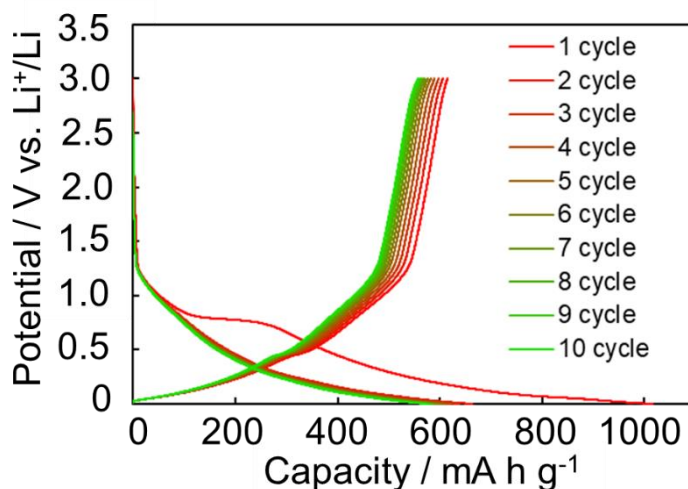employing a nonaqueous electrolyte, highlighting variations in behavior.

Figure 3-6. Charge/discharge curves of FeSi$_2$ electrode in 1 M LiPF$_6$/EC/EMC (30/70 vol.%).

Consequently, to unravel the reduction product after charge/discharge behavior and identify the anode material's involvement in the charge/discharge process, we scrutinized the XRD peaks of the electrodes after disassembling the evaluation cell at designated measurement points. Figure 3-7 illustrates a schematic of the cell dismantling process and its setup on the XRD measurement sample holder. Furthermore, Figure 3-8 shows the electrodes' appearance, while Table 3-2 details the cell voltage measurements after disassembly. The recorded electrode voltages during disassembly amounted to 1.632 V for Figure 3-5 (a), 0.140 V for Figure 3-5 (b), and 0.3664 V for Figure 3-5 (c). The XRD outcomes of the evaluation cells, subsequent to charge/discharge operations at 105 °C, and subsequent disassembly are displayed in Figure 3-9. Additionally, Figure 3-10 offers comprehensive data concerning the reaction phases identified in the XRD analysis.
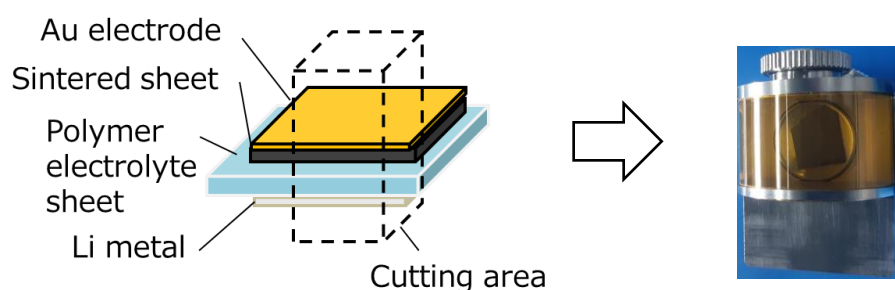

Figure 3-7. (Left) Schematic diagram of the cell and (right) XRD measurement sample holder containing the FeSi$_2$ sheet electrode.
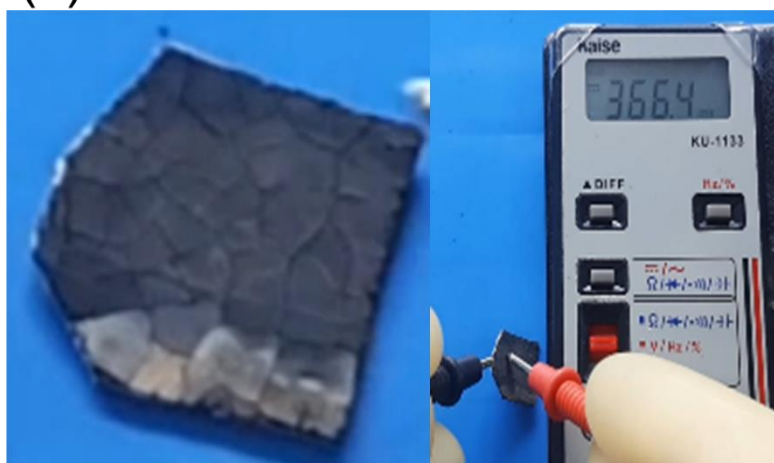
Figure 3-8. Exterior photographs of FeSi$_2$ sheet electrodes after (a) the first charge process at

630 mA h g^{-1}, (b) the third charge process at 0 V, and (c) the third discharge process at 3 V.

Table 3-2. The voltage of FeSi$_2$ electrodes after cell disassembly.

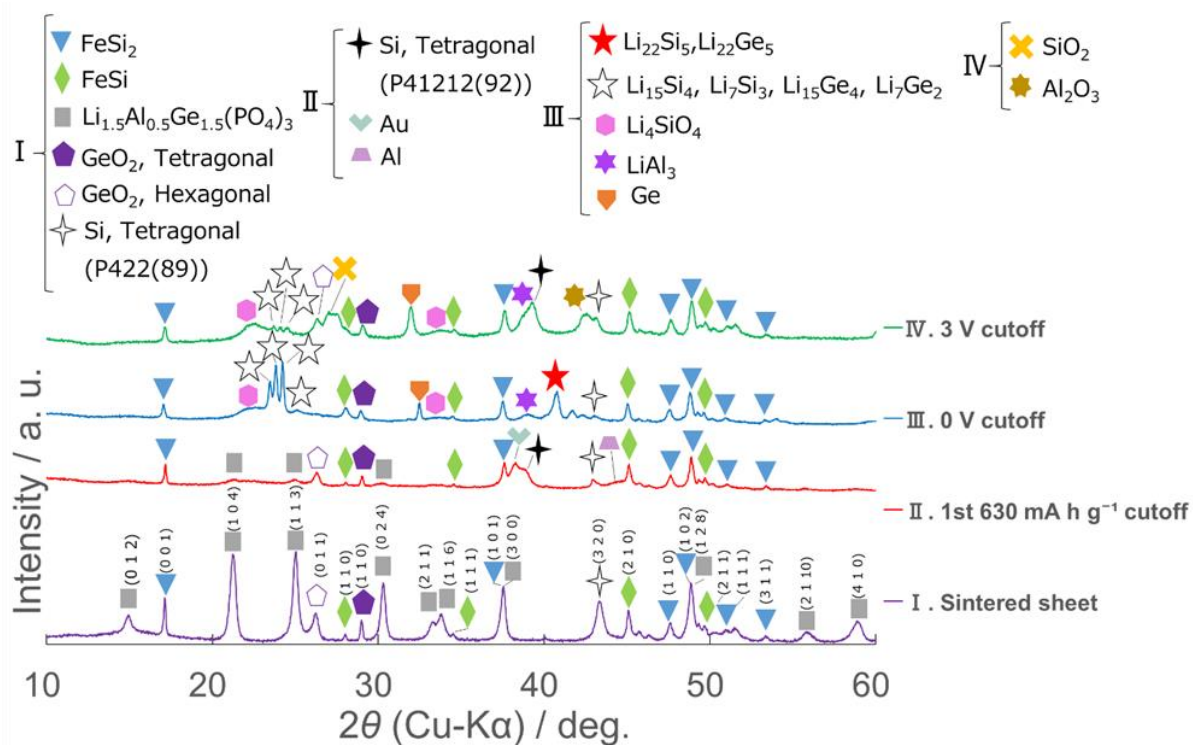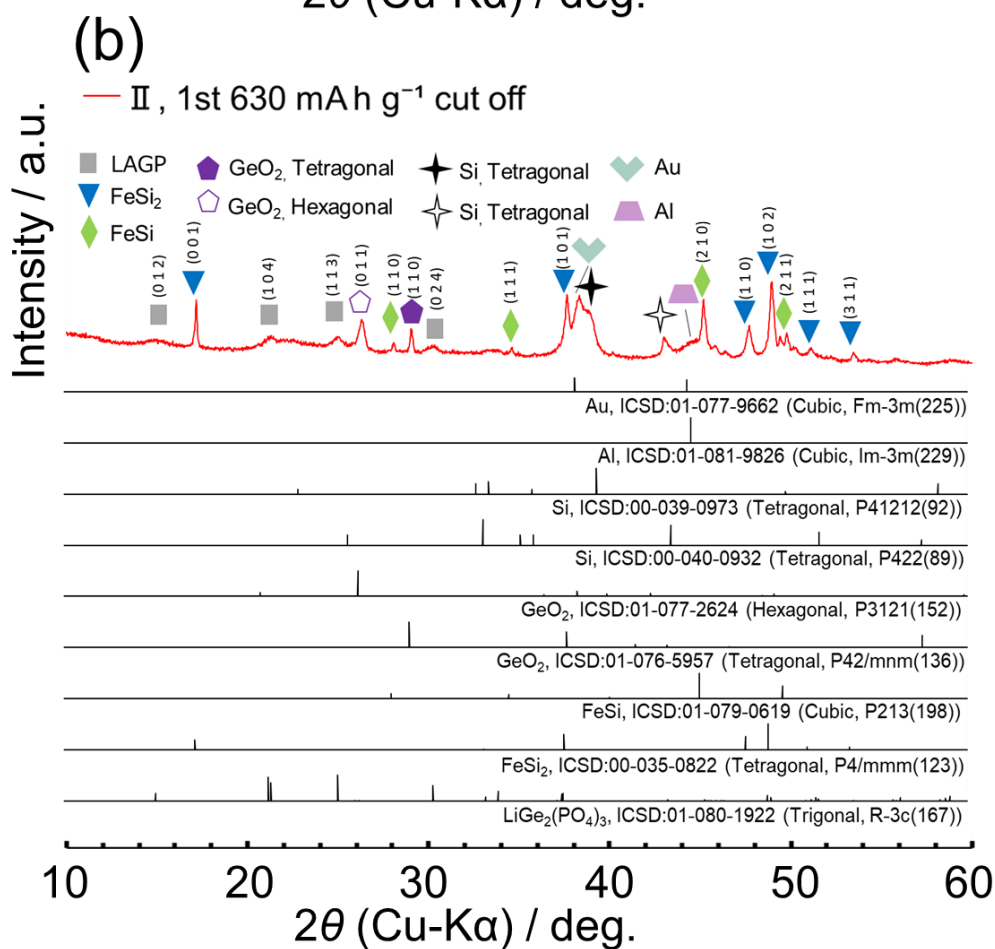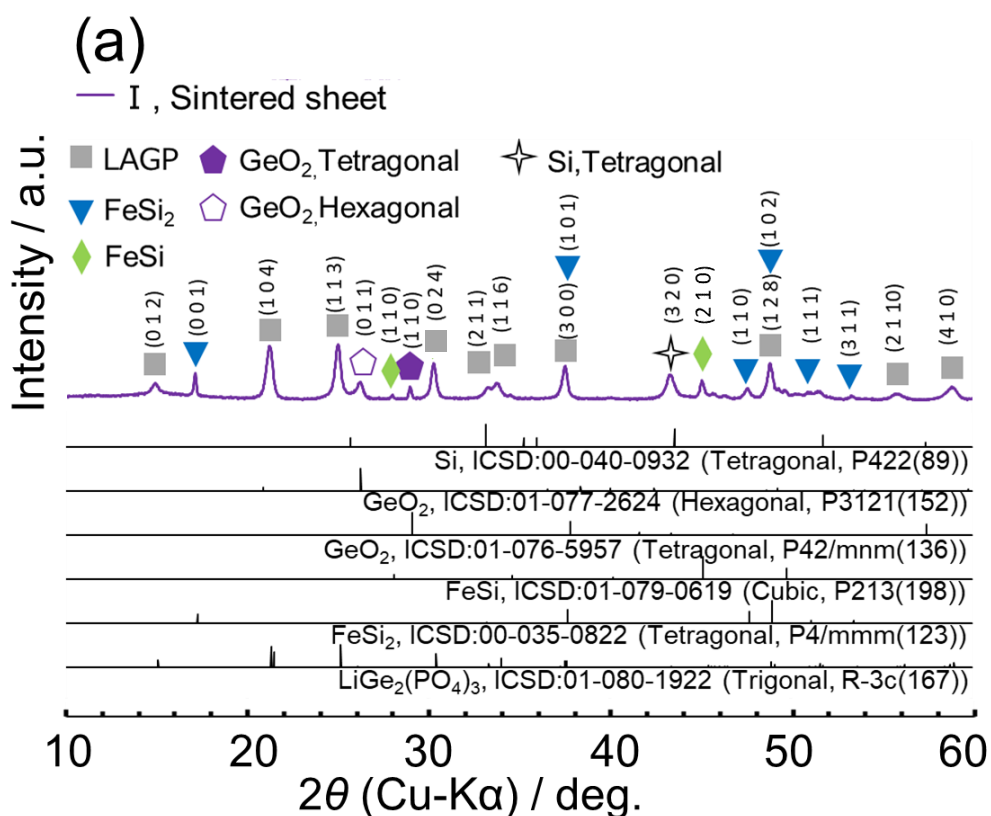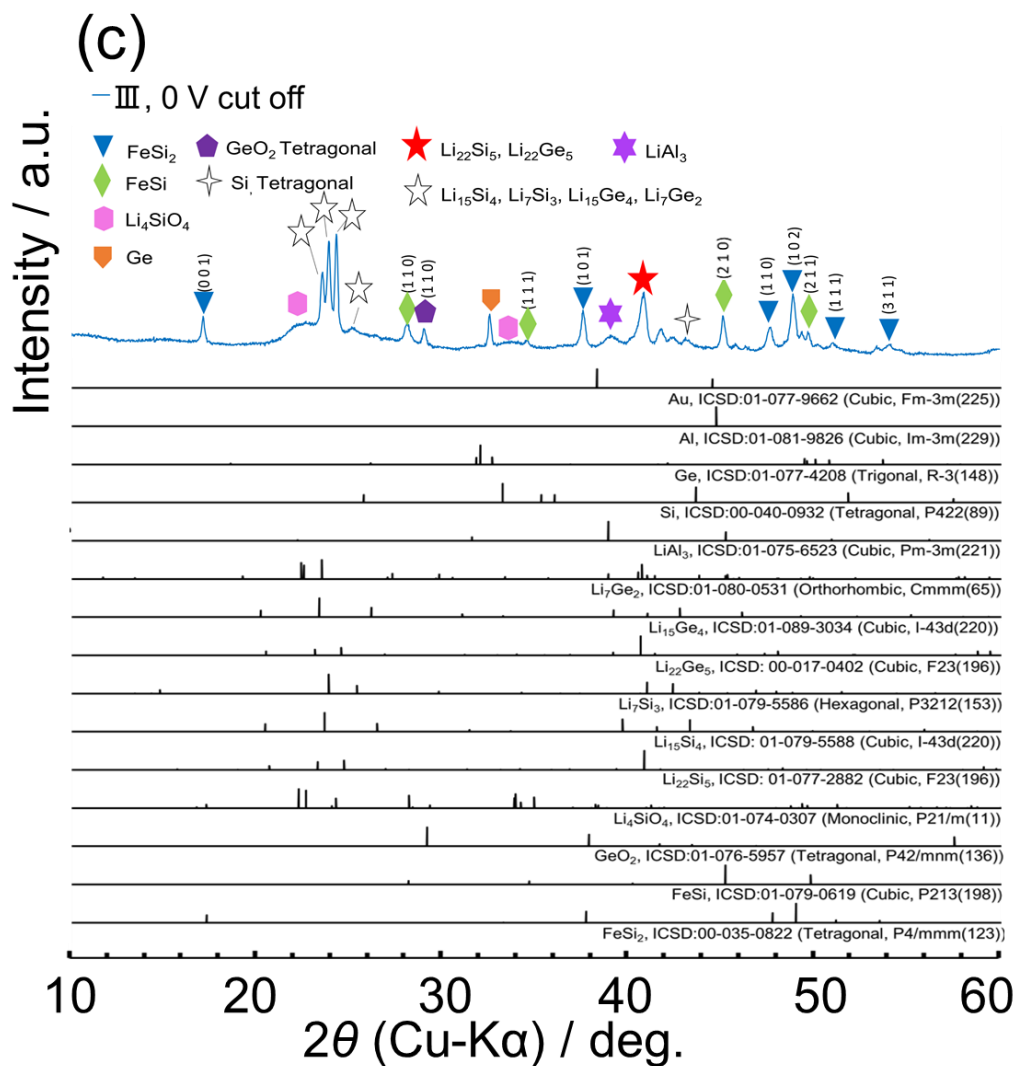| Disassembly sample	II. 630 mA h g^{-1} cut off	III. 0 V cut off	IV. 3 V cut off
Voltage (V)	1.632	0.140	0.3664

Figure 3-9. XRD patterns of sintered FeSi$_2$ sheet electrodes using after (a) the first charge process at 630 mA h g^{-1}, (b) the third charge process at 0 V, and (c) the third discharge process at 3 V.
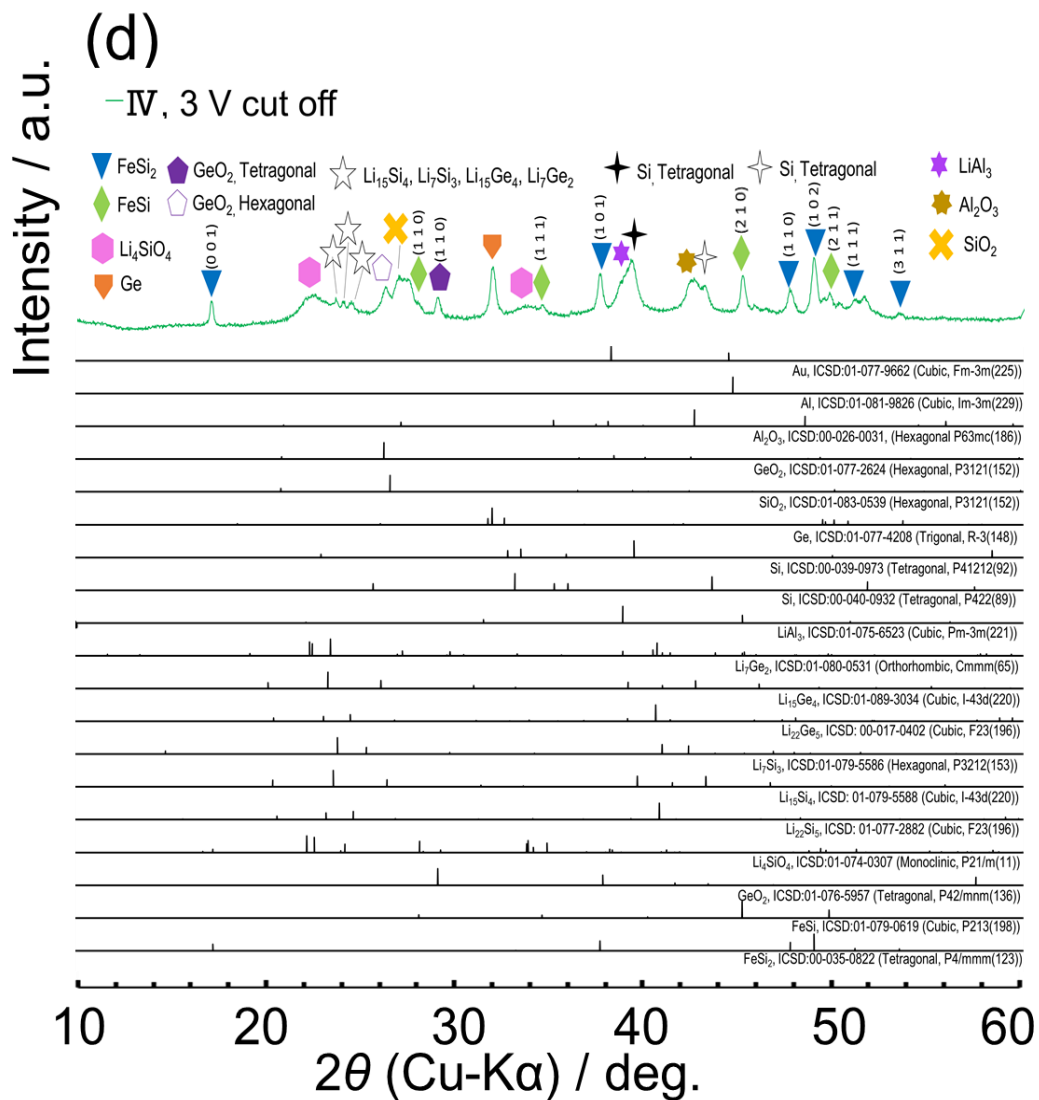
(c)

Ⅲ, 0 V cut off

▼ FeSi$_2$ ⬠ GeO$_2$ Tetragonal   ★ Li$_{22}$Si$_5$, Li$_{22}$Ge$_5$ ✦ LiAl$_3$

◆ FeSi   ✧ Si$_,$ Tetragonal   ☆ Li$_{15}$Si$_4$, Li$_7$Si$_3$, Li$_{15}$Ge$_4$, Li$_7$Ge$_2$

⬡ Li$_4$SIO$_4$

▼ Ge

Intensity / a.u.

(0 0 1) (1 1 0) (1 1 0) (1 1 1) (1 0 1) (2 1 0) (1 1 0) (1 0 2) (2 1 1) (1 1 1) (3 1 1)

Au, ICSD:01-077-9662 (Cubic, Fm-3m(225))

Al, ICSD:01-081-9826 (Cubic, Im-3m(229))

Ge, ICSD:01-077-4208 (Trigonal, R-3(148))

Si, ICSD:00-040-0932 (Tetragonal, P422(89))

LiAl$_3$, ICSD:01-075-6523 (Cubic, Pm-3m(221))

Li$_7$Ge$_2$, ICSD:01-080-0531 (Orthorhombic, Cmmm(65))

Li$_{15}$Ge$_4$, ICSD:01-089-3034 (Cubic, I-43d(220))

Li$_{22}$Ge$_5$, ICSD: 00-017-0402 (Cubic, F23(196))

Li$_7$Si$_3$, ICSD:01-079-5586 (Hexagonal, P3212(153))

Li$_{15}$Si$_4$, ICSD: 01-079-5588 (Cubic, I-43d(220))

Li$_{22}$Si$_5$, ICSD: 01-077-2882 (Cubic, F23(196))

Li$_4$SiO$_4$, ICSD:01-074-0307 (Monoclinic, P21/m(11))

GeO$_2$, ICSD:01-076-5957 (Tetragonal, P42/mnm(136))

FeSi, ICSD:01-079-0619 (Cubic, P213(198))

FeSi$_2$, ICSD:00-035-0822 (Tetragonal, P4/mmm(123))

10   20   30   40   50   60

2θ (Cu-Kα) / deg.

Figure 3-10. XRD patterns of sintered FeSi$_2$ sheets (a) as prepared, (b) after the first charge process at 630 mA h g^{-1}, (c) after the third charge process at 0 V, and (d) after the third discharge process at 3 V.

The XRD findings for the sintered sheet electrode are portrayed in Figure 3-9 I and Figure 3-10 (a). Consistent with the sintering test, the primary peaks corresponded to the LAGP phase and $FeSi_2$. Furthermore, the presence of FeSi was corroborated, initially part of the raw material mix. Notably, identified reaction phases encompassed GeO_2 (tetragonal), GeO_2 (hexagonal), and Si (tetragonal, space group P422(89)). This suggests that the addition of VGCF to the sintered sheet influenced the thermal conductivity within the material, potentially facilitating the formation of GeO_2 and Si.

Next, XRD measurement result II (Figure 3-10 (b)) within Figure 3-9, aimed at confirming structural shifts after initial charge, substantial alterations were noted. A significant reduction in the LAGP phase was evident. Additionally, there was a decrease in peak intensity and a shift in Si (tetragonal, space group P422(89)), with the emergence of Si peaks displaying a different space group (tetragonal, space group P41212(92)). This shift of the Si phase implies a structural transition to the Si phase, which is more likely to form alloys with Li. Moreover, the appearance of Al, absent prior to charging, was noted. The emergence of the gold (Au) peak from the current collector also corroborated the glossy Au surface observed in the disassembled cell (Figure 3-8 (a)). These outcomes indicate the concurrent reduction decomposition of LAGP and the formation of Si and Al phases during the initial Li insertion into the sintered sheet. Interestingly, the XRD peak of $FeSi_2$ remained unchanged

without any observed peak shift.

The analysis of XRD results III (Figure 3-10 (c)) in Figure 3-9, aimed at unveiling the products in the charged state at 0 V vs. Li$^+$/Li after three cycles, revealed significant transformations. Firstly, complete disappearance of the LAGP phase was confirmed. Secondly, peak intensities indicated the presence of alloy phases such as Li$_{22}$Si$_5$, Li$_{22}$Ge$_5$, Li$_{15}$Si$_4$, Li$_{15}$Ge$_4$, Li$_7$Si$_3$, and Li$_7$Ge$_2$, along with a phase resembling Li$_4$SiO$_4$ displaying a broad shape. Additionally, a phase representing LiAl$_3$ was identified. The GeO$_2$ (hexagonal) peak diminished compared to Stage II, while the GeO$_2$ (tetragonal) peak remained unchanged. Notably, peaks for Ge shifted to higher angles, while those for Al and Au phases vanished. This corresponded to a transformation of the gold electrode surface from gold to black (Figure 3-8 (b)). These outcomes indicate that Si, Ge, and Al were formed via reduction reactions of LAGP, FeSi$_2$, and GeO$_2$ (hexagonal) phases due to Li insertion up to 0 V vs. Li$^+$/Li. Moreover, it's suggested that an alloying reaction occurred between these metal elements and Li, demonstrating reversible charge/discharge reactions. Furthermore, the Li$_4$SiO$_4$ phase might have acted as a solid electrolyte, displaying conductivity at 100 °C.[53] Previous reports indicate that a solid solution of Li$_4$SiO$_4$-Li$_3$PO$_4$ exhibits Li conductivity.[54] Therefore, it's plausible that Li$_4$SiO$_4$ facilitated Li conduction in this electrode. Additionally, the XRD peak of FeSi$_2$ remained stable, suggesting its role as an anode material and electron conduction pathway,

further contributing to the charge/discharge reaction.

The XRD patterns of Stage IV in Figure 3-9, representing the discharge state at 3 V vs. $Li^{+/}Li$ after three cycles (Figure 3-10 (d)), highlight significant observations. The absence of $Li_{22}Si_5$ and $Li_{22}Ge_5$ phases and decreased intensities of $Li_{15}Si_4$, $Li_{15}Ge_4$, Li_7Si_3, and Li_7Ge_2 phases imply a reversal in the alloying reaction involving Si, Ge, Al, and Li. Instead, metallic Si and Ge or oxides like SiO_2, GeO_2, and Al_2O_3 were identified. This suggests that after the alloying reaction, metallic Si and Ge or their respective oxides were formed as Li was extracted. These findings strongly support the reversible charge/discharge reactions within the evaluation cell. Furthermore, investigating changes in charge/discharge behavior at different rates revealed interesting outcomes. When the rate was set at 0.02 C, the initial cycle displayed a plateau around 1.25 V vs. Li^+/Li during charging, similar to previous results. However, despite reaching a capacity of 630 mA h g^{-1}, no discharge behavior was observed. Moreover, there was no discernible plateau region around 0–1 V vs. Li^+/Li, indicating minimal charge/discharge behavior. Contrastingly, reducing the rate to 0.01 C led to the emergence of a plateau near 0–1 V vs. Li^+/Li, resulting in a reversible charge/discharge behavior of 400 mA h g^{-1}. This implies that the observed charge/discharge behavior is contingent upon sufficiently low current conditions. To investigate the charge/discharge reactuins in more detail, an electrode comprising solely LAGP and the conductive additive

VGCF (LAGP:VGCF = 90:10 wt%) was tested. However, no charge/discharge operations were observed (Figure 3-12). Additionally, cyclic voltammetry illustrated that the $FeSi_2$ sintered sheet exhibited higher current density than LAGP (Figure 3-13). Furthermore, a cell operated for ten cycles, with a charge capacity limit of 300 mA h g^{-1}, showed gradual improvement in reversible capacity (Figure 3-14). These collective results suggest that the $FeSi_2$ utilized in this study did not form a reaction phase with LAGP during co-sintering, retaining its electronic conductivity, thereby involving the charge/discharge behaviors.
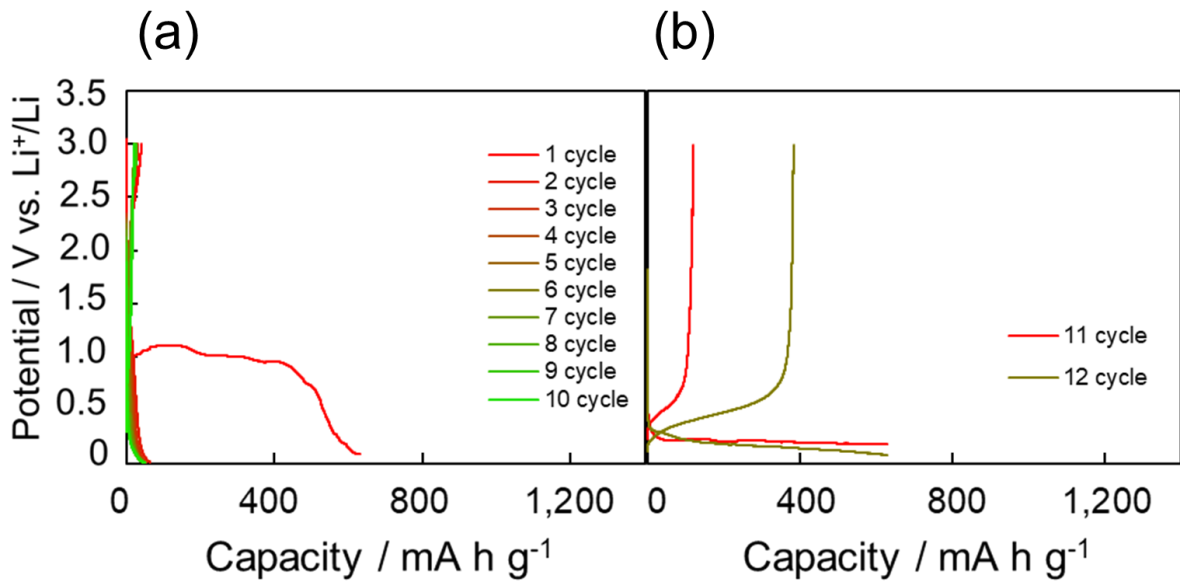

Figure 3-11. Charge/discharge curve of sintered $FeSi_2$ sheet electrodes after (a) 10 cycles at 0.02 C and (b) 2 cycles at 0.01 C.
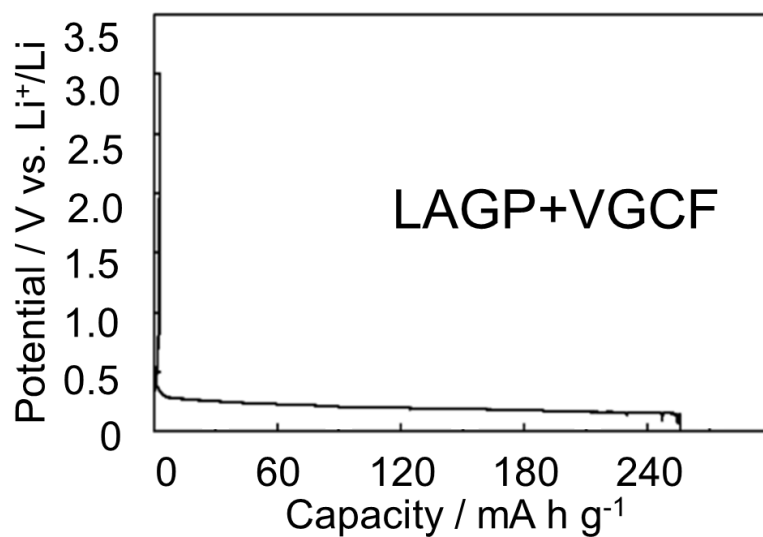
Figure 3-12. Charge/discharge curve of LAGP+VGCF at 0.01 C (1 C = 423 mA h g(LAGP)
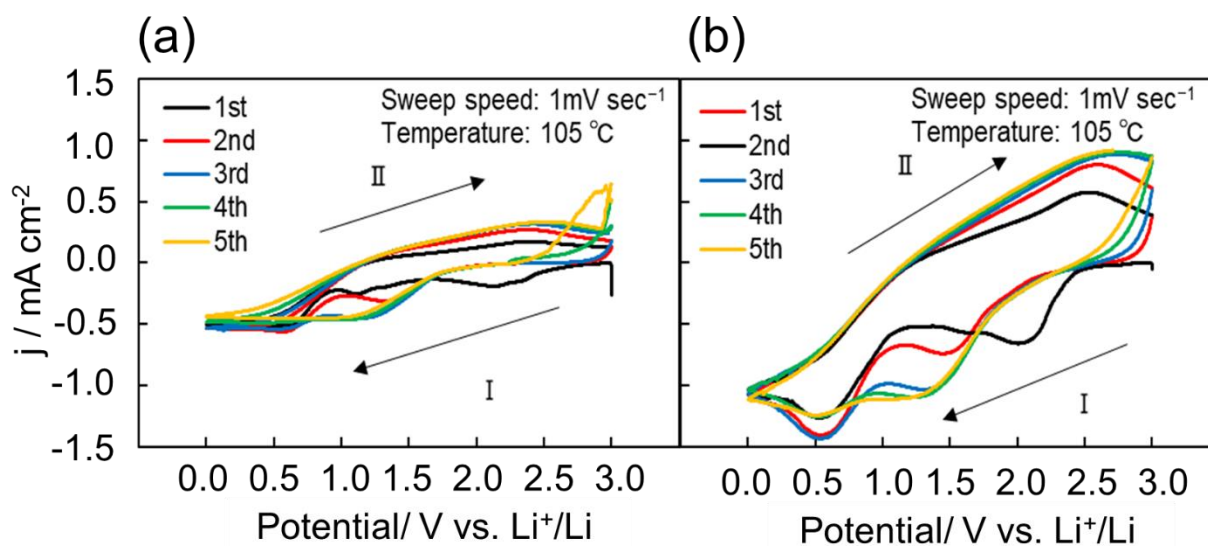
$^{-1}$ in constant current mode.

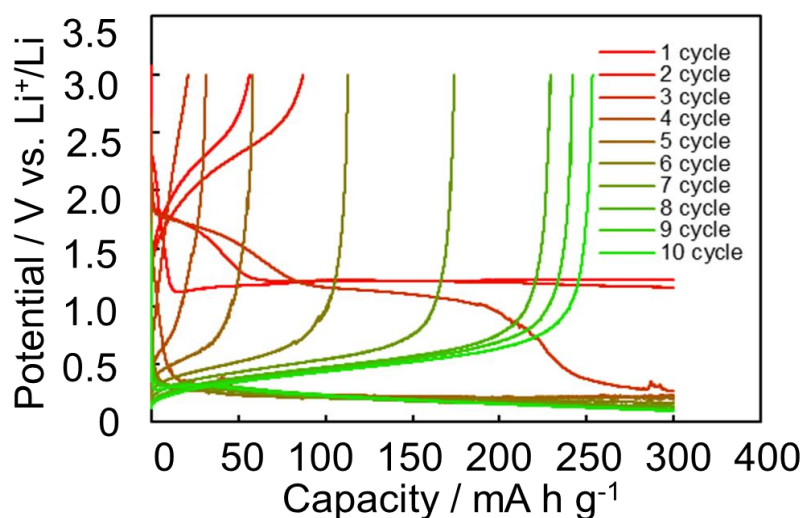Figure 3-13. Cyclic voltammograms of (a) LAGP+VGCF and (b) FeSi$_2$+LAGP+VGCF.

Figure 3-14. Charge/discharge curves of the FeSi$_2$ electrode with a charge capacity limitation

of 300 mA h g^{-1}.

The charge/discharge reaction can be hypothesized from these observations (Figure

3-15). Initially, LAGP experiences reduction and decomposition, leading to the creation of

Ge and Al. In our prior study, we detailed the redox behavior of LAGP sintered at 600 °C.[51]

The electronic density of states computations, based on first-principles calculations for

LAGP's constituent elements, suggest significant influence on Ge and O at the lowest position

of the conduction band on the reduction side. This indicates an anticipated reduction of GeO

and some implied reduction of P, without apparent involvement of Li in LAGP's reduction

decomposition at this stage. Previous findings suggested that during reduction decomposition,

LAGP initially forms small Ge particles surrounded by Li$_3$PO$_4$ and AlPO$_4$, leading to Ge's

alloying and de-alloying with Li.[23] This suggests the potential formation of Ge and other

metallic elements during LAGP's reduction decomposition, prompting de-insertion reactions

with lithium. Subsequently, a part of Si and $FeSi_2$ within the sintered sheet undergo reduction,

forming Si. Additionally, a Li insertion reaction involving Ge, Al, Si, and $FeSi_2$ enables them

to exhibit a reversible charge/discharge reaction. Li_4SiO_4 acts as a Li conductor in the

charge/discharge process. However, the charge/discharge capacity estimation is based on the

$FeSi_2$ quantity in the sintered sheet, making the involvement of Si and $FeSi_2$ in the process

uncertain. Further investigations are essential for a more comprehensive understanding of the
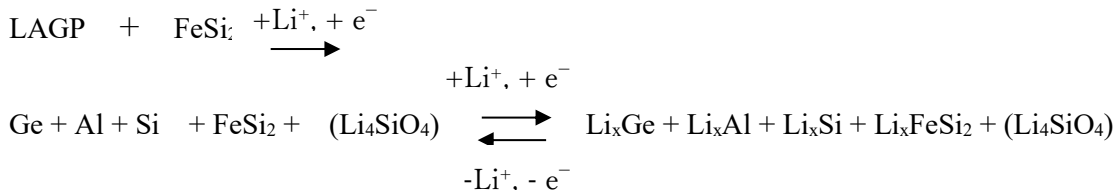
functional charge/discharge capacity.

$$LAGP \quad + \quad FeSi_2 \xrightarrow{+Li^+, + e^-}$$

$$Ge + Al + Si \ + FeSi_2 + \ (Li_4SiO_4) \quad \underset{-Li^+, - e^-}{\overset{+Li^+, + e^-}{\rightleftharpoons}} \quad Li_xGe + Li_xAl + Li_xSi + Li_xFeSi_2 + (Li_4SiO_4)$$

Figure 3-15. The reduction and charge/discharge reaction scheme of LAGP and $FeSi_2$

measuring the solid cell. (Substances in parentheses () indicate that they are not involved in

charge/discharge).

3.4 Summary

This study highlights the contribution of reduction decomposition products from the solid electrolyte in solid-state cells to reversible charge/discharge behavior. During co-sintering with the solid electrolyte LAGP, $FeSi_2$ showed minimal formation of reaction phases and retained an electronic conductivity of 10^{-3} S cm^{-1} after sintering. The charge/discharge outcomes from the solid-state cell using the sintered sheet achieved a reversible capacity of 400 mA h g^{-1}. After cell disassembly XRD results demonstrated the reduction and decomposition of LAGP, leading to the identification of Si, Ge, and Al as reduction decomposition products. It was assumed that the alloying phases of these elements with Li contributed to the charge/discharge reaction, alongside the generated Li_4SiO_4 acting as a Li conductor. The charge/discharge capacity estimated in this study was based on $FeSi_2$ present in the sintered sheet. The complex reactions make quantifying active materials challenging.

In our upcoming work, we plan to employ in-situ analysis with Raman spectroscopy, SEM, and energy dispersive X-ray spectrometry (EDS) to identify active materials in charge/discharge. This detailed analysis aims to determine the precise quantities of each substance, clarifying accurate charge/discharge capacity and reversible capacity. For long-term stability, managing the expansion and contraction of the sintered sheet is crucial, aiming

to create a structure enabling uniform charge/discharge reactions. Silicide alloys like $FeSi_2$, with excellent electronic conductivity, support uniform charge/discharge operation. We anticipate the potential of developing batteries featuring low electronic resistance, high energy density, and cost-effectiveness using $FeSi_2$ as an anode material.

Concluding Remarks

In this study, I summarizes research on NASICON-type solid electrolyte LAGP electrochemical properties in different sintering conditions and charge/discharge characteristics of titanium dioxide and silicide as anode materials after co-sintered with the solid electrolyte.

1   We describe the results of the investigation of the basic electrochemical properties of the oxide solid electrolytes used in sintered all-solid-state batteries. In this study, we evaluated the crystal structure and electrochemical properties of LAGP co-sintered at lower than 900 ℃ and confirmed appropriate sintering conditions. It was indicated that amorphous LAGP completely transformed to the crystalline phase when calcined at 800 ℃, and that the Li conductivity was significantly improved. However, the electrochemical stability of LAGP decreased, and oxidative decomposition progressed during charge/discharge reactions. This is thought to be due to the formation of vacancies in the crystal structure caused by the partial loss of Li in LAGP during sintering. On the other hand, when LAGP was sintered at 600 ℃, not only did it exhibit high Li conductivity, but also high electrochemical stability, as in the case of sintering at 800 ℃, although amorphous and crystalline LAGP phases were mixed. We speculate that the remaining amorphous phase suppressed the oxidative decomposition of the solid electrolyte.

2   We investigated that the charge/discharge characteristics of batteries prepared by co-sintering LAGP solid electrolyte and titanium dioxide (TiO_2) anode material at the temperature optimized in Chapter 1. XRD measurements clarified no reaction phases in the co-sintering process. In-situ measurements revealed the charge/discharge reaction behavior at the electrode-electrolyte interface. In this study, rutile-type TiO_2, which has the most stable crystal structure, was investigated. As a result, it was found that all-solid-state batteries using rutile-type TiO_2 as the anode electrode showed better input/output characteristics than those using anatase TiO_2. This was presumably due to the superior Li diffusion ability of rutile-type TiO_2. In-situ measurements of an all-solid-state battery during charge/discharge were also performed to visualize which part of the TiO_2 in the anode electrode layer absorbs and releases Li.

3   We demonstrated the analysis of LAGP solid electrolytes co-sintered with silicon and silicide-based anode materials, electronic conductivity before and after sintering, and charge/discharge characteristics of the fabricated batteries. As a result of co-sintering, crystalline phase reduced in the case of Si, SiO, and $NiSi_2$, and the electronic conductivity of $NiSi_2$ decreased to one billionth of its before sintering value. On the other hand, in the co-sintering test of $FeSi_2$, the formation observed no change and the electronic conductivity decreased by only about one-hundredth of a percent. In the charge/discharge test of the

sintered $FeSi_2$ electrode sheet, a potential plateau was observed at 1.25 V Li^+/Li, which was caused by the reduction of LAGP. Further charging to 0 V vs. Li^+/Li resulted in a discharge capacity of approximately 400 mA h g^{-1} derived from Li desorption. Ex-situ measurement of the electrode confirmed the disappearance of LAGP and the formation of Li-Si, Li-Ge and Li-Al alloyed phases and Li_4SiO_4, while $FeSi_2$ showed no change after charge/discharge. From these results, it can be inferred that LAGP is first reductively decomposed to form Ge and Al on the $FeSi_2$ electrode, then a part of $FeSi_2$ in the sintered compact is reduced to form Si, and Li is inserted into Ge, Al, Si and $FeSi_2$. The Li_4SiO_4 phase was considered to function as a Li conductor.

Acknowledgments

References

(1) Y.jin, Z. Zhap, S. Miao, Q.Wang, L. Sun, H. Lu, *J. Energy Strage.* **42**, 102987 (2021).

(2) Q. Wang, P. Ping, X. Zhao, G. Chu, J. Sun, C. Chen, *J. Power Sources*, **208**, 210 (2012).

(3) Z. J. Baum, R. E. Bird, X. Yu, J. Ma, *ACS Energy Lett*, **7**, 712 (2022).

(4) M. Pagliaro and F. Meneguzzo, *Heliyon,* **5**, 01866 (2019).

(5) C. Cao, Z. B. Li, X. L. Wang, X. B Zhao, W. Q. Han, *Front. Energy Res*, **2**, 25 (2014).

(6) F. Lv, Z. Wang, L. Shi, J. Zhu, K. Edstrom, J. Mindemark, S. Yuan, *J. Power Sources*, **441**, 227175 (2019).

(7) C. Z. Zhao, B. C. Zhao, C. Yan, X. Q. Zhang, J.Q. Huang, Y. Moc, X. Xu, H. Li, Q. Zhang, *Energy Strage Mater*, **24**, 75 (2020).

(8) R. Harada, K. Aso, A. Hayashi, M. Tatsumisago, *Electrochemistry*, **83**, 10, 898 (2015).

(9) A. M. Laptev, H. Zheng, M. Bram, M. Finsterbusch, O. Guillon, *Mat Lett*, **247**, 155 (2019).

(10) J. M. Valle and J. Sakamoto, *Solid State Ionics*, **345**, 115170 (2020).

(11) T. Ohtomo, A. Hayashi, M. Tatsumisago, Y. Tsuchida, S. Hama, K. Kawamoto, *J. Power Sources*, **233**, 231 (2013).

(12) M. Tatsumisago, F. Mizuno, A. Hayashi, *J. Power Sources*, **159**, 193 (2006).

(13) M. Xu, S. Song, S. Daikuhara, N. Matsui, S. Hori, K. Suzuki, M. Hirayama, S. Shiotani, S. Nakanishi, M. Yonemura, T. Saito, T. Kamiyama, R. Kanno, *Inorg. Cheme.*, **61**, 52 (2022).

(14) Y. Zhu, Y. Zhang, L. Lu, *J. Power Sources*, **290**, 123 (2015).

(15) M.Foucaud, S. Renka, T. Klaser, J. Popovi´c, Ž. Skoko, P. Mošner, L. Koudelka, A. Šanti´c, *Nano Mater.*, **12**, 240 (2022).

(16) H. Yamauchi, J. Ikejiri, K. Tsunoda, A. Tanaka, F. Sato, T. Honma, T. Komatsu, *Nature.*, **10**, 9453 (2020).

(17) M. Chen, W. Hua, J. Xiao, D. Cortie, W. Chen, E. Wang, Z. Hu, Q. Gu, X. Wang, S. Indris, S. L. Chou, S. X. Dou, *Nat. Commun.*, **10**, 9453 (2020).

(18) X. Yan, Z. Wang, M. He, Z. Hou, T. Xia, G. Liu, X. Chen, *Energy Technol.*, **3**, 801 (2015).

(19) Z. Sun, S. Tao, X. Song, P. Zhang, L. Gao, *J. Am. Chem. Soc.* **162**, 8, A1530 (2015).

(20) J. Zhao, H. W. Lee, J. Sun, Y. Cui, *Pnas.* **113**, 27, 7408 (2016).

(21) C. Yamamoto, S. Doi, M. Nakanishi, M. Kobayashi, M. Inagaki, Y. Goto, J. Kato, K. Yamamoto, A. Kato, Y. Kataoka, Abstracts of, *PRiME2020*, A05-0911 (2020).

(22) M. Kotobuki, M. Koishi, *J. Asian Ceram. Soc.,* **7**, 551 (2019).

(23) J. K. Feng, L. Lu, M. O. Lai, *J.Alloys Compd.,* **501**, 255 (2010).

(24) Y. Benabed, M. Rioux, S. Rousselot, G. Hautier, M. Dollé, *Front. Energy Res.,* **9**, 682008 (2021).

(25) Z. Liu, S. Venkatachalam, H. Kirchhain, L. V. Wüllen, *Solid State Ionics*, **295**, 32 (2016).

(26) S. V. Pershina, A. A. Pankratov, E. G. Vovkotrub, B. D. Antonov, *Ionics*, **25**, 4713 (2019).

(27) A. Curcio, A. G. Sabato, M. N. Eroles, J. C. G. R, A. Morata, A. Tarancón, F. Ciucci, *ACS Appl. Energy Mater.*, **5**, 14466 (2022).

(28) A. M. Rodriguesa, J. L. Narváez-Semanatea, A. A. Cabralb, A. C. M. Rodrigues, *Mater. Res.,* **16**, 4, (2013).

(29) P. Gorai, H. Long, E. Jones, S. Santhanagopalan, Vladan Stevanovic, *J. Mater. Chem. A*, **8**, 3851 (2020).

(30) H. Usui, Y. Domi, S. Ohnishi, H. Sakaguchi, *ACS Appl. Nano Mater*., **2**, 5360 (2019).

(31) T. Ohtomo, A. Hayashi, M. Tatsumisago, Y. Tsuchida, S. Hama, K. Kawamoto, *J. Power Sources*, **233**, 231 (2013).

(32) H. Yamada and K. Takemoto, *Solid State Ionics,* **285**, 41 (2016).

(33) Y. Kawano, A. Kato, H. Usui, Y. Domi, H. Sakaguchi, *Electrochemistry*, **91**, 6, 067003 (2023).

(34) H. Kim, S. Lee, Y-U. Park, H. Kim, J. Kim, S. Jeon, K. Kang, *Chem. Mater*, **23**, 17, 3930 (2011).

(35) S. Patoux, C. Masquelier, *Chem. Mater.*, **14**, 12, 5057 (2002).

(36) H. Usui, Y. Domi, S. Ohnishi, N. Takamori, S. Izaki, N. Morimoto, K. Yamanaka, K.

Kobayashi, H. Sakaguchi, *ACS Materials Lett*, **3**, 372 (2021).

(37) G. Okuma, N. Saito, K. Mizuno, Y. Iwazaki, H. Kishi, A. Takeuchi, M. Uesugi, K. Uesugi, F. Wakai, *Acta Mater*, **206**, 116605 (2021).

(38) H. Masuda, N. Ishida, Y. Ogata, D. Ito, D. Fujita, *J. Power Sources*, **400**, 527 (2018).

(39) C. K. Christensen, M. A. H. Mamakhel, A. R. Balakrishna, B. B. Iversen, Y. M. Chiang, D. B. Ravnsbæk, *Nanoscale*, **11**, 12347 (2019).

(40) H. Usui, Y. Domi, T. H. Nguyen, S. Izaki, K. Nishikawa, T. Tanaka, H. Sakaguchi, *Electrochemistry*, **90**, 3, 037002 (2022).

(41) H. Usui, Y. Domi, S. Ohnishi, S. Izaki, A. Nasu, A. Sakuda, A. Hayashi, H. Sakaguchi, *J. Phys. Chem. C*, **126**, 10320 (2022).

(42) D. Ma, Z. Cao, A. Hu, *Nano-Micro Lett*, **6**, 4, 347 (2014).

(43) G. G. Eshetu, H. Zhang, X. Judez, H. Adenusi, M. Armand, S. Passerini, E. Figgemeier, *Nat. Commun.*, **12**, 5459 (2021).

(44) Y. Domi, H. Usui, K. Yamaguchi, S. Yodoya, H. Sakaguchi, *ACS Appl. Mater. Interfaces*, **11**, 2950 (2019).

(45) Y. Domi, H. Usui, N. Ieuji, K. Nishikawa, H. Sakaguchi, *ACS Appl. Mater. Interfaces*, **13**, 3816 (2021).

(46) Y. Domi, H. Usui, K. Nishikawa, H. Sakaguchi, *ACS Appl. Nano Mater.*, **4**, 8473 (2021).

(47) Y. Domi, H. Usui, K. Sugimoto, K. Gotoh, K. Nishikawa, H. Sakaguchi, *ACS Omega*, **5**, 22631 (2020).

(48) Y. Domi, H. Usui, T. Ando, H. Sakaguchi, *Mater. Adv.*, **3**, 6231 (2022).

(49) I. A. Tarasov, I. A. Bondarev, A. I. Romanenko, *J. Surf. Invest.*, **14**, 4, 851 (2020).

(50) Y. Domi, H. Usui, R. Takaishi, H. Sakaguchi, *ChemElectroChem*, **6**, 581 (2019).

(51) Y. Kawano, A. Kato, H. Usui, Y. Domi, H. Sakaguchi, *Electrochemistry*, **91**, 9, 097004 (2023).

(52) E. Shoko, Y. Dang, G. Han, B. B. Duff, M. S. Dyer, L. M. Daniels, R. Chen, F. Blanc, J. B. Claridge, M. J. Rosseinsky, *Inorg. Chem.* **60**, 18, 14083 (2021).

(53) S. B. R. S. Adnan and N. S. Mohamed, *Ceram. Int*., **40**, 7, 11441 (2014).

(54) Y. Deng, C. Eames, J. Chotard, F. Lal re, V. Seznec, S. Emge, O. Pecher, C. P. Grey, C. Masquelier, M. S. Islam, *J. Am. Chem. Soc*. **137**, 9136 (2015).

List of Publications

[1] NASICON-type $Li_{1.5}Al_{0.5}Ge_{1.5}(PO_4)_3$ Containing Amorphous Phase for Solid Li-Ion Conductor

<u>Y. Kawano</u>, A. Kato, H. Usui, Y. Domi, H. Sakaguchi, *Electrochemistry*, **91** (2023) 097004-097009.

[2] TiO_2 Anode Material for All-Solid-State Battery Using NASICON $Li_{1.5}Al_{0.5}Ge_{1.5}(PO_4)_3$ as Lithium Ion Conductor

<u>Y. Kawano</u>, A. Kato, H. Usui, Y. Domi, H. Sakaguchi, *Electrochemistry*, **91** (2023) 067003-067008.

[3] Electrochemical Anode Behavior of α-$FeSi_2$ co-Sintered with Solid Electrolyte

<u>Y. Kawano</u>, A. Kato, H. Usui, Y. Domi, H. Sakaguchi, *Electrochemistry*, **92** (2024) 017004-017010.

Supplementary Publication

[1] Development of Anode Material for Oxide-based All-Solid-State Battery

<u>Y. Kawano</u>, A. Kato, H. Usui, Y. Domi, H. Sakaguchi, *Electrochemistry,* **91,** 4 (2023) 382-387.